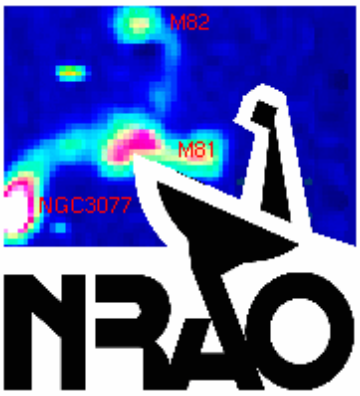

GBT Memo #311

X-band Receiver Technical Memo

Walter Klahold

Green Bank Observatory

wklahold@nrao.edu

May 28, 2024

Abstract

A new X-band receiver has been designed and commissioned for use at the GBT Gregorian focus, and expands the frequency coverage of the previous GBT X-band receiver from nominally 8-10 GHz to 8-12 GHz. This memo discusses the technical aspects of the upgraded GBT X-band receiver, including the results and testing methodology of lab measurements of certain key components (e.g. LNAs, feed horn, etc.) and performance characteristics of the receiver as a whole (e.g. receiver temperature, gain stability, cooldown time, etc.).

Change Record

Revision	Date	Author	Sections/Pages Affected
	Remarks		
1.0	2023-Oct-05	W. Klahold	All
	Initial version		

Contents

1. Introduction

In November of 2022, a new X-band receiver was installed at the GBT Gregorian focus as a complete replacement for the previous GBT X-band receiver. As can be seen in the block diagram shown in Figure 1, the new receiver, like its predecessor, consists of a single, dual circularly polarized feed, a pair of cryogenic low noise amplifiers (LNAs) followed by a single heterodyne downconversion mixing stage at room temperature, and a pair of noise diodes for either "high" or "low" power calibrated noise injection to the LNA inputs (see Table 2 for identification information on the components in the block diagram). However, the overall receiver bandwidth has been expanded from nominally 8-10 GHz to nominally 8-12 GHz, due predominantly to the use of a turnstile orthomode transducer (OMT) as the polarizing element (labeled W6 in Figure 1).

On-sky commissioning for the new X-band receiver took place between the end of 2022 and the end of 2023, the details of which have been documented in the corresponding commissioning report (Morgan 2023). The purpose of this memo is to summarize certain key performance aspects of the receiver itself as determined from laboratory measurements. These include both system-level characteristics such as receiver temperature and gain stability as well as the performance characteristics of certain key components such as the feed horn and cryogenic LNAs. A summary of the system-level characteristics is given in Table 1, while additional details are given in the following sections. Other topics addressed in this memo include radio frequency interference (RFI) considerations (particularly those related to downlinks from low-earth-orbit (LEO) satellite constellations), monitor and control functions and hardware, and troubleshooting. Throughout this memo, reference will occasionally be made to archived drawings and other documents relating to the upgraded X-band receiver or other systems, which can be found in the directory `/doc/drawings/archive/gbelectronics/` on the Green Bank database server, `leo.gb.nrao.edu`.

Table 1. Summary of X-band receiver's nominal performance characteristics

Performance characteristic	Value
Nominal bandwidth	8 - 12 GHz
Receiver noise temperature	10 - 25 K
Low cal noise temperature	2 - 3 K
High cal noise temperature	6 - 12 K
Total receiver gain	90 dB
Receiver 1 dB output power compression point	16 dBm
Received power flux density at 1 dB compression	180 Jy over 4 GHz
Fractional gain stability at $\tau = 0.2$ s	3×10^{-4}
IF center frequency (wideband mode)	4 GHz
IF center frequency (narrowband mode)	6 GHz
Feed polarization	Dual circular
Feed edge taper	11 - 14 dB
Receiver cross-polarization	$<$ -20 dB
Cooldown time	16 hours
Warmup time (with heaters)	10 hours

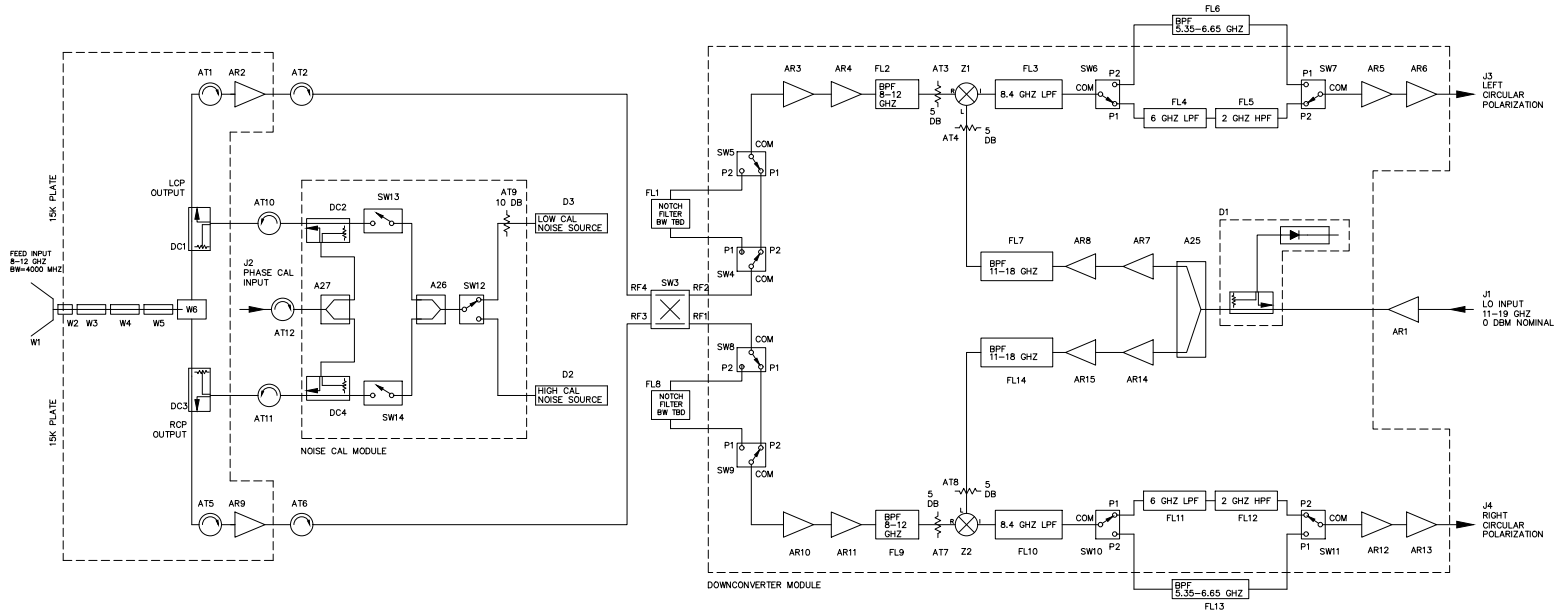

Fig. 1.— Block diagram for the RF electronics portion of the new GBT X-band receiver. Identification information for all components is given in Table 2

Table 2. Parts list for components shown in RF block diagram in Figure 1

Designator	Type	Manufacturer	Part no. / description	Serial no.
AR1	Amplifier	X-Microwave	XM-A2A5-0404C	12000
AR2	Amplifier	NRAO	X-band cryo LNA	048
AR3	Amplifier	X-Microwave	XM-A9W5-0404D	27902
AR4	Amplifier	X-Microwave	XM-A9W5-0404D	27903
AR5	Amplifier	X-Microwave	XM-C7D7-0404D	64035
AR6	Amplifier	X-Microwave	XM-C7D7-0404D	64036
AR7	Amplifier	X-Microwave	XM-A3E6-0404D	27927
AR8	Amplifier	X-Microwave	XM-A9R7-0404D	29819
AR9	Amplifier	NRAO	X-band cryo LNA	049
AR10	Amplifier	X-Microwave	XM-A9W5-0404D	29823
AR11	Amplifier	X-Microwave	XM-A9W5-0404D	29824
AR12	Amplifier	X-Microwave	XM-C7D7-0404D	64037
AR13	Amplifier	X-Microwave	XM-C7D7-0404D	64038
AR14	Amplifier	X-Microwave	XM-A3E6-0404D	29834
AR15	Amplifier	X-Microwave	XM-A9R7-0404D	29820
FL1	Filter	TBD	TBD	TBD
FL2	Filter	X-Microwave	XM-A2B3-0404D	27904
FL3	Filter	X-Microwave	XM-A1H3-0204D	27907
FL4	Filter	X-Microwave	XM-A9J9-0404D	27909
FL5	Filter	X-Microwave	XM-A1D4-0204D	27911
FL6	Filter	X-Microwave	XM-B6N2-0604C	62902
FL7	Filter	X-Microwave	XM-A265-0604D	27925
FL8	Filter	TBD	TBD	TBD
FL9	Filter	X-Microwave	XM-A2B3-0404D	27905
FL10	Filter	X-Microwave	XM-A1H3-0204D	27908
FL11	Filter	X-Microwave	XM-A9J9-0404D	27910
FL12	Filter	X-Microwave	XM-A1D4-0204D	27912
FL13	Filter	X-Microwave	XM-B6N2-0604C	62903
FL14	Filter	X-Microwave	XM-A265-0604D	54745
SW3	Switch	X-Microwave	XM-B8C6-0409D	27923
SW4	Switch	X-Microwave	XM-B6H9-0409D	27894
SW5	Switch	X-Microwave	XM-B1C9-0409D	27898
SW6	Switch	X-Microwave	XM-B6H9-0409D	27895

Table 2—Continued

Designator	Type	Manufacturer	Part no. / description	Serial no.
SW7	Switch	X-Microwave	XM-B1C9-0409D	27899
SW8	Switch	X-Microwave	XM-B1C9-0409D	27900
SW9	Switch	X-Microwave	XM-B6H9-0409D	27896
SW10	Switch	X-Microwave	XM-B1C9-0409D	27901
SW11	Switch	X-Microwave	XM-B6H9-0409D	27897
SW12	Switch	X-Microwave	XM-B6H9-0409D	31966
SW13	Switch	X-Microwave	XM-A5A8-0404D	31959
SW14	Switch	X-Microwave	XM-A5A8-0404D	31958
W1	Waveguide	GBO	Corrugated feed horn	-
W2	Waveguide	GBO	Thermal transition	-
W3	Waveguide	GBO, NRAO	Circ. to square transition	001
W4	Waveguide	GBO, AJ Tuck	90 deg. phase shifter	001
W5	Waveguide	GBO, NRAO	45 deg. twist	001
W6	Waveguide	NRAO	Turnstile OMT	-
AT1	Isolator	Raditek	RADI-8.0-12.4-Cryo-(4-77K)-WR90-1WR	106
AT2	Isolator	RF-Lambda	RFLI601G08G12	-
AT5	Isolator	Raditek	RADI-8.0-12.4-Cryo-(4-77K)-WR90-1WR	107
AT6	Isolator	RF-Lambda	RFLI601G08G12	-
AT10	Isolator	RF-Lambda	RFLI601G08G12	-
AT11	Isolator	RF-Lambda	RFLI601G08G12	-
AT12	Isolator	RF-Lambda	RFLI601G08G12	-
DC1	Coupler	A-Info	90WL+CS-30_CU	J506062770
DC2	Coupler	X-Microwave	XM-B9Y3-0404D	31968
DC3	Coupler	A-Info	90WL+CS-30_CU	J506062771
DC4	Coupler	X-Microwave	XM-A2Y3-0404D	31957
AT3	Attenuator	X-Microwave	XM-A234-0204D	29828
AT4	Attenuator	X-Microwave	XM-A234-0204D	29829
AT7	Attenuator	X-Microwave	XM-A234-0204D	29830
AT8	Attenuator	X-Microwave	XM-A234-0204D	29831
AT9	Attenuator	X-Microwave	XM-B4Y2-0204D	31967
Z1	Mixer	X-Microwave	XM-B2D4-0404D	27906
Z2	Mixer	X-Microwave	XM-B9G3-0404D	29827
D1	Detector	X-Microwave	XM-B7R4-0404D	29832

Table 2—Continued

Designator	Type	Manufacturer	Part no. / description	Serial no.
D2	Diode	NoiseCom	NC3206	AK366
D3	Diode	NoiseCom	NC3206	AK367
A25	Power Divider	X-Microwave	XM-A3R3-0604D	31962
A26	Power Divider	X-Microwave	XM-A3R3-0604D	31964
A27	Power Divider	X-Microwave	XM-A3R3-0604D	31963

2. Receiver and noise diode noise temperature measurements

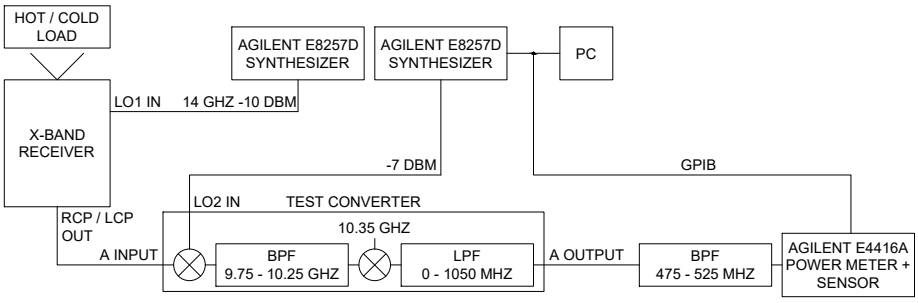

Fig. 2.— Test setup used for measuring X-band receiver noise temperature. Block diagram for test converter has been simplified. Refer to archived drawing C35240K003 for additional details.

The X-band receiver noise temperature has been measured in the lab using the setup shown in Figure 2. In this setup, the y-factor method is used to calculate the receiver temperature according to the equations:

$$T_{rx} = \frac{T_H - Y T_C}{Y - 1}, \tag{1}$$

$$Y = \frac{P_H}{P_C}, \tag{2}$$

where $T_H = 290$ K and $T_C = 81$ K are the respective hot and cold load temperatures and P_H and P_C are the respective measured output power detected at the power sensor. The resolution bandwidth is limited in this case to 50 MHz by the final bandpass filter, and the measurement frequency f_{sky} is set by the LO2 synthesizer frequency f_{LO2} according to the relation

$$f_{sky} = f_{LO1} - (f_{LO2} - (f_{LO3} - 500\,\mathrm{MHz})), \tag{3}$$

where $f_{LO1} = 14$ GHz, $f_{LO3} = 10.35$ GHz, and 500 MHz is the center frequency of the final bandpass filter. The results of these measurements are shown for the right-circularly-polarized (RCP) and left-circularly-polarized (LCP) channels in Figures 3 and 4, respectively. In this case, f_{LO1} is fixed at 14 GHz to center the IF on 4 GHz, and the receiver has been configured in its wideband mode (2-6 GHz IF filters selected, see Section 5) such that the full 8-12 GHz receiver bandwidth can be downconverted to a fixed IF center frequency for measuring T_{rx}. Once T_{rx} has been measured, either the low cal or high cal noise diode is turned on, and the noise temperature contribution from the corresponding noise diode can be calculated similarly to (1):

$$T'_{rx} = T_{rx} + T_{cal} = \frac{T_H - Y' T_C}{Y' - 1}, \tag{4}$$

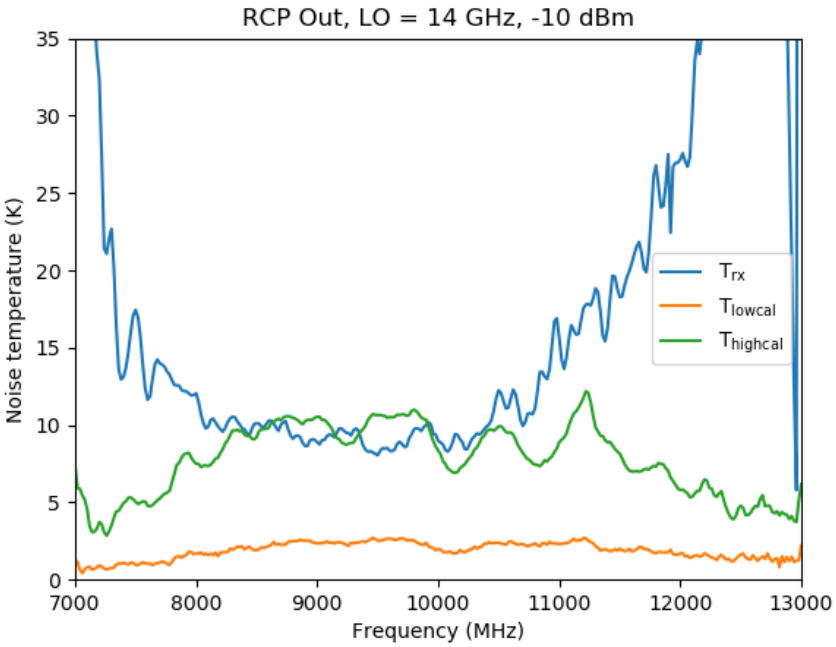

Fig. 3.— Measured noise temperature for receiver and low and high cal noise diodes for the RCP channel. The receiver was put into its wideband mode, with the IF centered on 4 GHz and 2 - 6 GHz IF bandpass filters selected.

$$T_{cal} = \frac{T_H - Y'T_C}{Y' - 1} - T_{rx}. \tag{5}$$

From Figures 3 and 4 it is seen that T_{rx} varies from its minimum of about 10 K in the range 8-10 GHz to about 30 K at 12 GHz (note: there is still appreciable sensitivity down to about 7.3 GHz). The increase with frequency can be readily understood to be a consequence of the receiver's cryogenic LNAs. Across the 8-12 GHz band, their gain steadily decreases with increasing frequency, while for frequencies above about 11 GHz their noise temperature also increases by a few Kelvin (see Figure 17 in Section 8). Attenuation in the transmission lines between the cryogenic LNAs and the first room temperature stage of amplifiers in the receiver's downconverter module will also increase with frequency, thus compounding the effect of the LNA gain rolloff.

It should be pointed out that one significant source of systematic error in these noise temperature measurements is the uncertainty in the hot and cold load temperatures T_H and T_C. The hot load is an absorber assumed to be at ambient room temperature, which may drift by a few Kelvin over the course of a measurement. The cold load is an absorber immersed in a liquid nitrogen bath. Ideally, its temperature should be well-stabilized at the boiling point of nitrogen, 77 K. However, in practice it has been found that the effective cold load temperature is closer to 81 K, likely due incomplete coverage of the load over the feed or radiative heat transfer from the warm Styrofoam

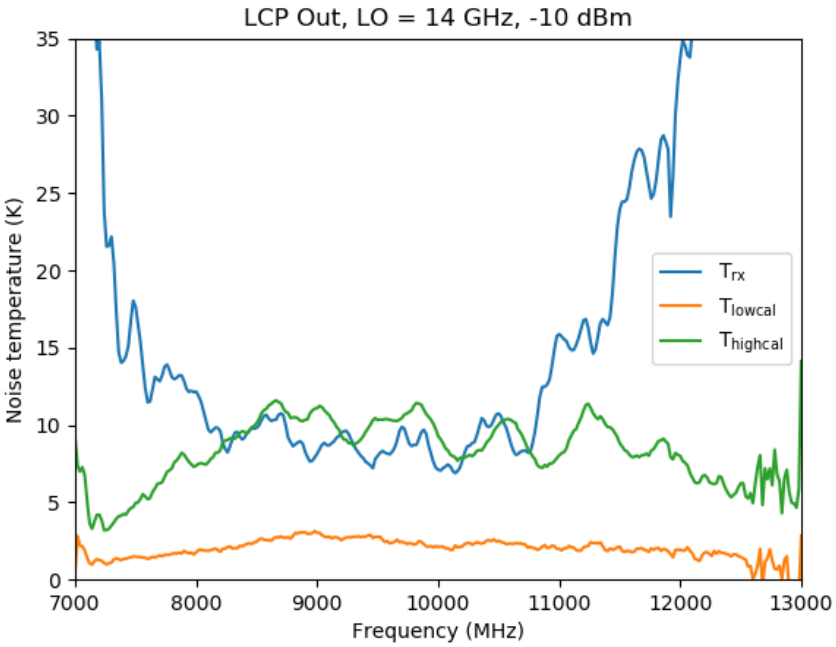

Fig. 4.— Measured noise temperature for receiver and low and high cal noise diodes for the LCP channel. The receiver was put into its wideband mode, with the IF centered on 4 GHz and 2 - 6 GHz IF bandpass filters selected.

container for the immersed absorber. The net uncertainty in T_{rx} is expected to be within a few Kelvin.

3. Receiver gain and linearity

Table 3 shows the nominal gain for each component in the receiver as well as the total total gain of the receiver, ∼90 dB. The receiver linearity was assessed by injecting a test tone at the phase cal input to the receiver and varying its power level until saturation of the output power was observed. A block diagram of the test setup is shown in Figure 5 and a plot of the results is shown in Figure 6.

From these data it was determined that, for this setup, 1 dB of output compression occurred at an output power level of about +10 dBm, as measured at the output of the 20 MHz wide bandpass filter. The abscissa of Figure 6 includes both the injected tone power (referenced to the cryogenic LNA input) as well as the noise power due to the receiver and the 300 K absorber placed over the feed, the latter of which produced about -9 dBm at the output of the 20 MHz wide bandpass filter when the test tone was turned off. Assuming uniform power spectral density across the receiver's

Table 3. Nominal gain for each component in the X-band receiver. It is assumed the receiver is configured in its wideband mode (i.e. the downconverter module's internal IF filters are selected for a nominal IF center frequency of 4 GHz). Component designators refer to Figure 1.

Component	Designator	Gain (dB)
Waveguides	W1-W6, DC1/DC2	-0.5
Cryogenic isolator	AT1/AT5	-0.5
Cryogenic LNA	AR2/AR9	35
Coax	-	-2.0
Isolator	AT2/AT6	-0.5
Transfer switch	SW3	-0.7
Notch filter switch 1	SW4/SW8	-1
Transmission line	-	-0.8
Notch filter switch 2	SW5/SW9	-1
RF amplifier 1	AR3/AR10	15
RF amplifier 2	AR4/AR11	15
RF filter	FL2/FL9	-2
5 dB attenuator	AT3/AT7	-5
Mixer	Z1/Z2	-11
Low pass filter	FL3/FL10	-0.5
IF filter switch 1	SW6/SW10	-1
Low pass filter	FL4/FL11	-0.5
High pass filter	FL5/FL12	-3.0
Transmission line	-	-0.2
IF filter switch 2	SW7/SW11	-1
IF amplifier 1	AR5/AR12	27
IF amplifier 2	AR6/AR13	27
Total	-	87.8

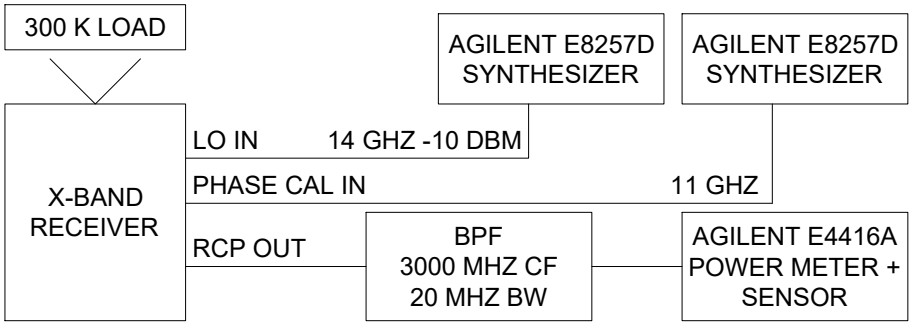

Fig. 5.— Test setup for measuring receiver linearity

4 GHz bandwidth, the total output power measured directly at the receiver output would be

$$\begin{aligned} P_{total} =& P_N + P_{tone} \\ =& \left(-9\,\mathrm{dBm} + 10\log_{10}\frac{4\,\mathrm{GHz}}{20\,\mathrm{MHz}}\right) + 10\,\mathrm{dBm} \\ =& 16\,\mathrm{dBm}. \end{aligned} \tag{6}$$

This is equal to the nominal 1 dB compression point of the final IF amplifier stage, indicating it is the limiting element to the receiver linearity. Assuming that the nominal receiver gain is 90 dB, the corresponding input power level is -74 dBm, which if distributed uniformly over the 4 GHz receiver bandwidth in turn corresponds to 720 K noise temperature or a 180 Jy power flux density at the GBT (assuming an aperture efficiency of 70%).

4. Gain stability

For a receiver with perfect gain stability, the radiometer equation predicts that the fractional uncertainty in the receiver output power P will decrease with $(\Delta\nu\tau)^{-1/2}$, where $\Delta\nu$ is the effective bandwidth of the signal at the power detector input and τ is the effective integration time. If, however, the gain G fluctuates over the course of this integration, an excess uncertainty in the output power will result:

$$\frac{\Delta P}{P} = \sqrt{\frac{1}{\Delta\nu\tau} + \left(\frac{\Delta G}{G}\right)^2}. \tag{7}$$

The test setup for measuring the receiver gain stability is shown in Figure 7. In this setup, the receiver is configured in its "narrowband" mode (see Section 5), where the LO is set to 16 GHz to downconvert the nominal 8-12 GHz bandwidth to a 6 GHz IF center frequency and the receiver's internal IF filters are selected, which have a 6 GHz center frequency and 1.3 GHz bandwidth. The receiver's RCP output is connected to a spare optical driver module (identical to those in

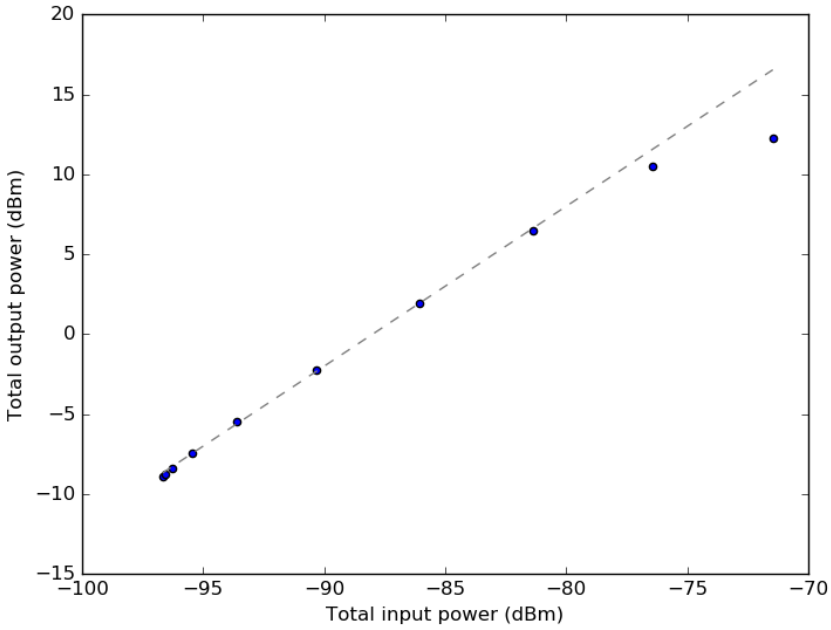

Fig. 6.— Results of receiver linearity measurements for an injected test tone at 11 GHz (see Figure 5 for measurement setup). The measured 1 dB compression point at the receiver occurred in this case for an output power of +10 dBm (in a 20 MHz bandwidth). The dashed line is a linear fit to the data excluding the last three points, where saturation begins to occur.

the GBT IF rack) with its internal attenuator set to 17 dB and internal bandpass filter set to a 6 GHz center frequency and 80 MHz bandwidth (the 17 dB attenuator was selected for optimal linearity and signal-to-noise ratio at the video amplifier output, for which the voltage is nominally 1 V). Averaging the receiver output power was accomplished by connecting a counter to the V/F converter output, which produced a pulse train whose repetition rate is proportional to the receiver output power. The counter was configured for an integration time of $\tau_0 = 10$ ms, and after each integration the count total was polled and stored on a computer over the course of 100 seconds (N =10,000 samples).

To use the measured power to estimate the fractional power uncertainty as a function of integration time τ, we take its estimator to be the overlapping Allan deviation $\sigma_y(n\tau_0, N)$:

$$\sigma_y^2(n\tau_0, N) = \frac{1}{2n^2\,(N-2n+1)} \sum_{j=0}^{N-2n} \left(\sum_{i=j}^{j+n-1} y_{i+n} - y_i \right)^2, \tag{8}$$

$$y_i = \frac{P_i}{\bar{P}}, \tag{9}$$

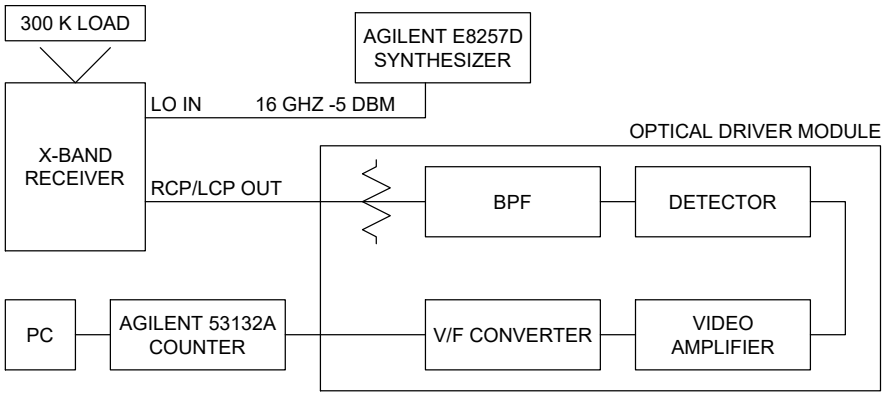

Fig. 7.— Test setup for measuring continuum gain stability. For the measurement results shown in Figure 8, the attenuator was set to 17 dB and the selected bandpass filter had a 6 GHz center frequency and 80 MHz bandwidth. The counter was configured in totalize mode with a 10 ms integration time.

$$\bar{P} = \frac{1}{N}\sum_{i=0}^{N-1} P_i. \tag{10}$$

Here, the Allan deviation is evaluated for the integration time τ_0 of the time series P_i and estimated for integration times τ equal to integer multiples of τ_0 up to the full 100 s duration of the time series. A plot of the Allan deviation is shown in Figure 8.

From the plot it can be seen that for short integration times, the Allan deviation closely follows the $(\Delta\nu\tau)^{-1/2}$ dependence predicted by the radiometer equation[1], but above integration times of approximately 0.1 s the $\Delta G/G$ term of Equation (8) begins to predominate. Here, $\Delta G/G$ is calculated by rearranging Equation (7) as follows:

$$\begin{aligned}\frac{\Delta G}{G} &= \sqrt{\left(\frac{\Delta P}{P}\right)^2 - \frac{1}{\Delta\nu\tau}} \\ &\approx \sqrt{\sigma_y^2 - \frac{1}{\Delta\nu\tau}},\end{aligned} \tag{12}$$

where the approximation is meant to emphasize that σ_y is a statistical estimator that converges

[1]The bandwidth $\Delta\nu$ used here is determined by the optical driver module bandpass filter (see Figure 7). It is not the 3 dB bandwidth (80 MHz), but the effective pre-detection bandwidth defined by (Tiuri 1964):

$$\Delta\nu = \frac{\left(\int_0^\infty df G(f)\right)^2}{\int_0^\infty df G^2(f)}, \tag{11}$$

where $G(f)$ is the filter (power) gain. $\Delta\nu$ was calculated to be 106 MHz using the measured filter response and integration limits of 5 and 7 GHz. The integration carried out by the counter is assumed to be ideal, and so the effective integration time τ_0 is equal to the counter integration time, 10 ms.

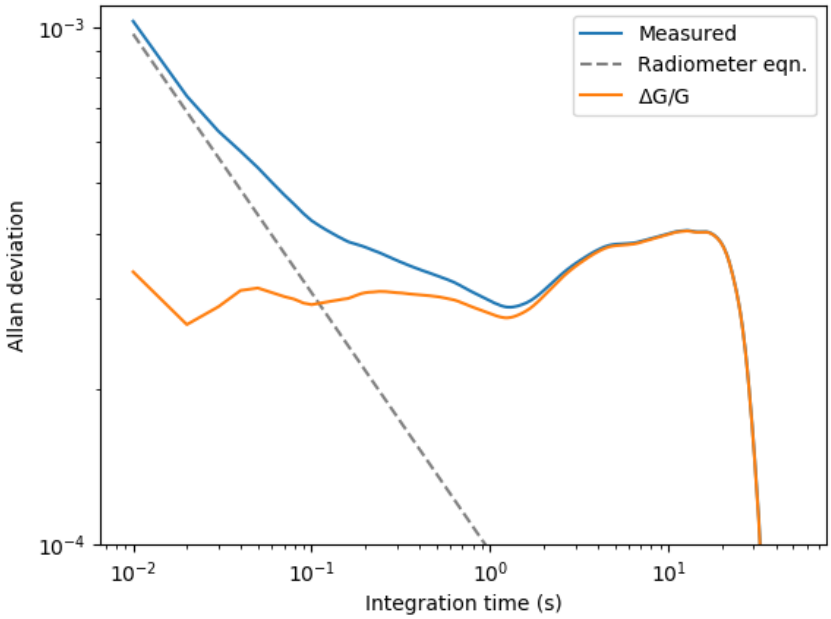

Fig. 8.— Measured Allan variance of the receiver output power for the setup shown in Figure 7. The dashed line shows the expected dependence as predicted by the radiometer equation (Equation (7) with $\Delta G = 0$).

to $\Delta P/P$ for large N. The τ dependence of the $\Delta G/G$ term can be further subdivided into two regimes: flicker $(1/f)$ noise, which is constant with τ and predominates up to about $\tau \approx 1$ s, and random walk noise, which has a $\tau^{1/2}$ dependence and predominates beyond $\tau \approx 1$ s. The strong dropoff in both σ_y and $\Delta G/G$ at large τ is due to the limited number of large τ intervals into which the original time series can be subdivided, thus producing a low-confidence estimate for $\Delta P/P$.

For comparison with the gain stability measurements of the previous GBT X-band receiver, we consider the Allan deviation at an integration time $\tau = 0.2$ s (sample rate $f_s = 5$ Hz). From the plot it can be determined that $\Delta G/G$ at $\tau = 0.2$ s is equal to $\sim 3 \times 10^{-4}$, whereas for the previous GBT X-band receiver it was determined to be $(6.9 \pm 1.5) \times 10^{-4}$ (Mason 2013).

5. IF center frequency

Both the new and old GBT X-band receivers are of a heterodyne configuration with the LO "high-side" injected into a single mixing stage, whereupon the receiver's input bandwidth is downconverted to a nominal IF center frequency. On the GBT, two standard IF center frequencies are available to heterodyne receivers: 3 GHz and 6 GHz. These frequencies are determined by the two

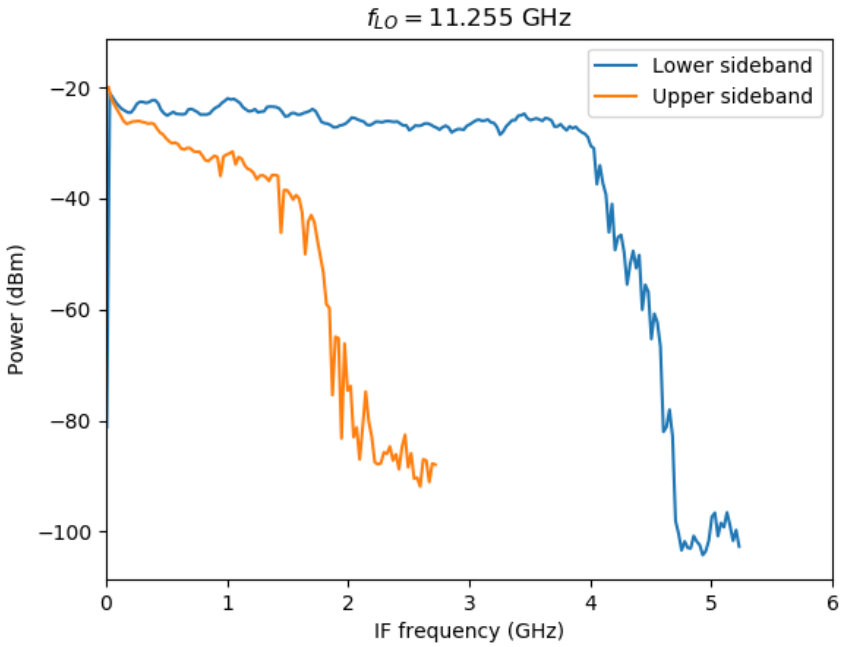

Fig. 9.— Measured IF output of X-band receiver downconverter module with a fixed LO frequency of 11.255 GHz for both the lower sideband (downconverter input frequency f_{RF} swept through 6.025-11.250 GHz, output measured at frequency $f_{IF} = f_{LO} - f_{RF}$) and upper sideband (downconverter input frequency f_{RF} swept through 11.275-13.975 GHz, output measured at frequency $f_{IF} = f_{RF} - f_{LO}$). IF filters internal to downconverter have been bypassed to demonstrate image rejection level at IF frequencies < 2 GHz. The input power to the downconverter was kept at a constant -80 dBm.

sets of filter banks internal to the IF rack, to which the receiver outputs are first routed before being sent to the converter racks and backends. Whereas the old receiver was designed around a nominal 3 GHz IF center frequency, a different choice was made for the new receiver in light of its expanded bandwidth. The reason a 3 GHz IF center frequency was not chosen was to improve image rejection, which decreases with decreasing IF center frequency. This is because, for high-side injection, the LO must be tuned closer to the upper end of the receiver input bandwidth as the IF center frequency decreases, in which case signal in the upper band edge of the input bandwidth may be present in both the upper and lower sidebands of the LO. Two signals at the image frequencies

$$\begin{aligned} f_u &= f_{LO} + f_{IF}, \\ f_l &= f_{LO} - f_{IF} \end{aligned} \tag{13}$$

will therefore be downconverted to the same IF frequency f_{IF}. For small f_{IF}, the mixer conversion loss is fairly equal between the upper and lower sidebands of the LO, and so the signals at the image frequencies may appear in roughly equal magnitude. An extreme case of this can be seen in

Figure 9 where the LO frequency is tuned within the input bandwidth of the receiver. Therefore, if the IF frequency is brought higher such that the LO is far enough away from the receiver input bandwidth, image rejection can be greatly improved.

On the other hand, a 6 GHz IF center frequency is also not ideal. The reason for this is that, in general, mixers have some finite amount of signal that passes from the RF input to the IF output without having been mixed with the LO. This is called "RF breakthrough," and as was the case above, it also has the effect of superimposing two signals at different frequencies in the receiver's input bandwidth onto the same IF frequency. A plot showing the relative magnitude of the RF breakthrough in comparison to the lower sideband is shown in Figure 10. Here it can be seen that, at an IF frequency of 6 GHz, the RF breakthrough is approximately -60 dB relative to the lower sideband, but rapidly climbs to about -30 dB at an IF frequency of 8 GHz.

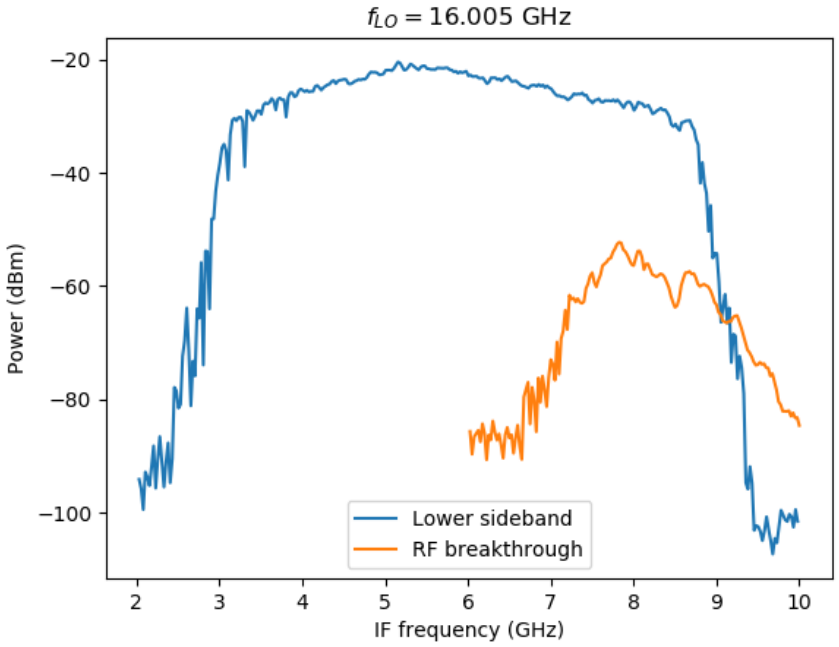

Fig. 10.— Measured IF output of X-band receiver downconverter module with a fixed LO frequency of 16.005 GHz for both the lower sideband (downconverter input frequency f_{RF} swept through 6.025-13.975 GHz, output measured at frequency $f_{IF} = f_{LO} - f_{RF}$) and the RF breakthrough (input frequency f_{RF} swept through 6.025-10.000 GHz, output measured at frequency $f_{IF} = f_{RF}$). IF filters internal to downconverter have been bypassed to demonstrate RF breakthrough level at IF frequencies > 6 GHz. Rolloff at high frequency end of RF breakthrough due to 9 GHz low pass filter immediately following mixer, which was not bypassed. The input power to the downconverter was kept at a constant -80 dBm.

In order to maintain good image rejection while minimizing RF breakthrough, it was therefore

determined that the receiver should be designed to have both a "narrowband" and "wideband" mode, which correspond to different choices of IF center frequency and IF filters. In narrowband mode, the nominal IF center frequency is 6 GHz, but the IF filters internal to the receiver and the IF rack are chosen to have bandwidths that reject those IF frequencies for which RF breakthrough increases above some minimum level. The maximum bandwidth in this case is 1.3 GHz, and is limited by the two of the receiver's IF filters connected externally to the receiver downconverter module (FL6 and FL13 in Figure 1). In wideband mode, the IF center frequency is set nominally to 4 GHz, and the bandwidth is limited to 4 GHz by the downconverter module's internal IF filters (FL4, FL5, FL11, and FL12 in Figure 1). In this latter case, since a 4 GHz center frequency is not compatible with either filter bank in the IF rack, the IF rack must be configured in its "all pass" or "thru" state. In practice, this selection process is handled automatically by the GBT config tool. Further details can be found in the X-band receiver's commissioning report (Morgan 2023).

6. Feed pattern and phase center

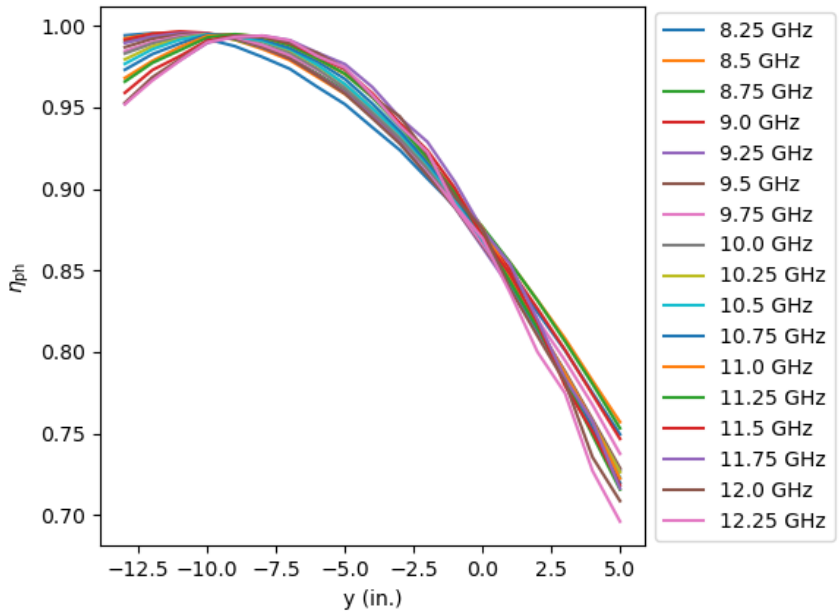

Fig. 11.— Measured feed horn phase efficiency η_{ph} versus frequency and center of rotation y.

The feed horn radiation pattern and phase center were determined in the Green Bank Observatory anechoic chamber. The phase center was determined first by measuring the phase efficiency at several different frequencies between 8 and 12 GHz as a function of the position y of the feed's center of rotation along its boresight axis (see drawing 300002A022 for a description of the coordinate

system). For a fixed frequency and rotation axis, the phase efficiency was determined numerically from the corresponding measured E- and H-field co-polar radiation patterns $E_E(\psi)$ and $E_H(\psi)$ using the following relation (see appendix to Thomas 1971):

$$\eta_{ph} = \frac{\left| \int_0^{\Psi} [E_E(\psi) + E_H(\psi)] \tan\frac{\psi}{2} d\psi \right|^2}{\left\{ \int_0^{\Psi} [|E_E(\psi)| + |E_H(\psi)|] \tan\frac{\psi}{2} d\psi \right\}^2}, \tag{14}$$

where ψ is the rotation angle of the feed horn axis with respect to the anechoic chamber transmitter's axis and Ψ is the half-angle subtended by the GBT subreflector, which is 15 degrees. From these data, curves showing phase efficiency versus center of rotation could be produced for fixed frequency, as shown in Figure 11. From this, the phase center position at each frequency was taken to be the maximum of each of these curves as determined from a fit to a parabola. The determined phase center positions are shown for each of the measurement frequencies in Figure 12. Given that point/focus scans at X-band are typically carried out at 9 GHz, the X-band receiver was designed such that the corresponding phase center determined from Figure 12 is coplanar with the top face of the turret hole cover, which in turn coincides with the Gregorian focal point of the GBT subreflector.

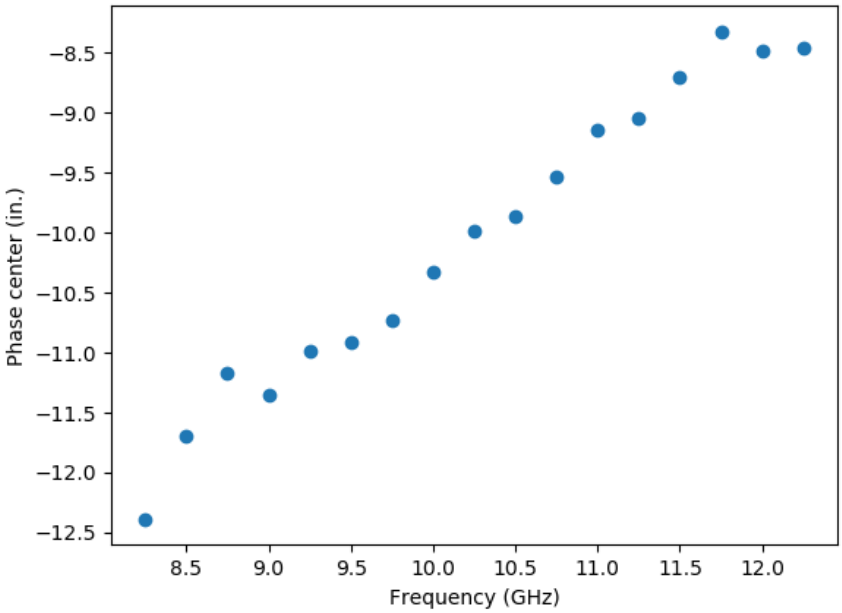

Fig. 12.— Measured feed horn phase center position versus frequency as determined from the maxima in the curves shown in Figure 11

With the phase center having been determined as a function of frequency, the co-polar and cross-

polar radiation patterns of the feed horn were measured in the E-, H-, and D-plane with the center of rotation placed sequentially at $y = -12.392$, -10.837, and -8.481 inches, corresponding to the phase centers at 8 GHz, 10 GHz, and 12 GHz, respectively. The E-plane co-polar radiation patterns are shown in Figure 13. The edge taper in the E- and H-planes decreases with increasing frequency in the range 11 to 14 dB, and is due in part to the increasing presence of higher order modes with increasing frequency (note the bilobate structure appearing at 12 GHz in the inset to Figure 13). Both the gross features of the measured radiation patterns as well as the observation of higher order modes agree with results of electromagnetic field simulations carried out in CST, indicating no issues with fabrication. The 11 to 14 dB edge taper is also close to the 15 dB edge taper found to optimize the GBT gain-to-T_{sys} ratio at 5 GHz (Norrod and Srikanth, 1996). Note: the optimal edge taper trends lower with increasing frequency.

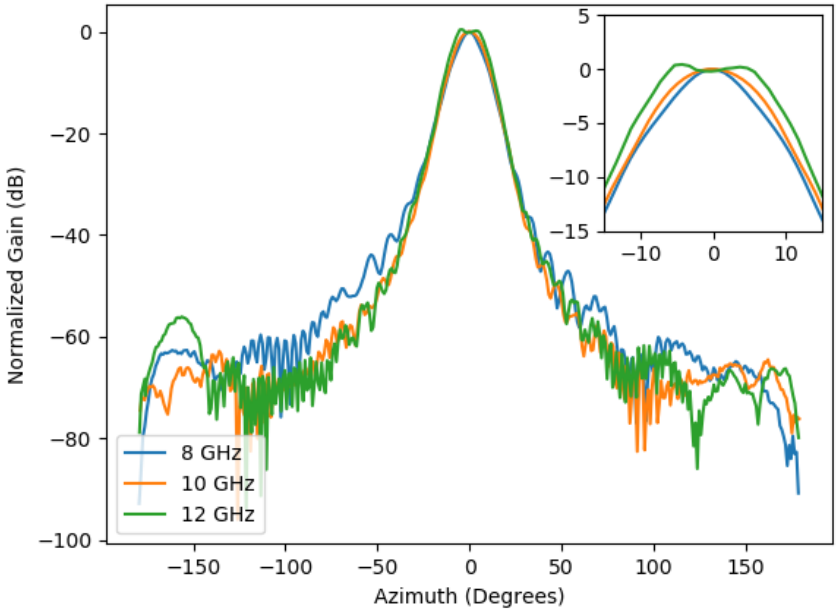

Fig. 13.— Measured feed horn E-plane co-polar radiation pattern at frequencies $f = 8$, 10, and 12 GHz. Inset shows an expanded view of the radiation pattern within the ±15 degree limits of the GBT subreflector. A transition to a bilobate pattern is observed at 12 GHz indicating the presence of higher order modes.

7. Polarization

7.1. Convention

As mentioned, the X-band receiver natively detects right- and left-circular polarization. However, before discussing the polarization properties of the X-band receiver, it is worth stating explicitly which of the two possible handedness conventions is to be used. One is the IEEE convention, which states: "the sense of polarization, or handedness ... is called right handed (left handed) if the direction of [electric field] rotation is clockwise (anti-clockwise) for an observer looking in the direction of propagation" (ANSI/IEEE 1979). The opposite convention, which occurs more frequently in the field of optics, interchanges the definition of right- and left-circular polarization, and can be stated similarly to the above definition but with the substitution that one looks in the direction of the source of the radiation rather than the direction of propagation. Mathematically, these definitions can be expressed in terms of the corresponding plane-wave electric fields propagating in the $+z$-direction:

$$\vec{E}_R^{(IEEE)} = \vec{E}_L^{(Optics)} = (E_0/\sqrt{2})(\vec{x} + i\vec{y}) \exp\left[2\pi i(z - ct)/\lambda\right], \tag{15}$$

$$\vec{E}_L^{(IEEE)} = \vec{E}_R^{(Optics)} = (E_0/\sqrt{2})(\vec{x} - i\vec{y}) \exp\left[2\pi i(z - ct)/\lambda\right], \tag{16}$$

where E_0 is the electric field magnitude, i is the imaginary unit, c is the speed of light, and λ is the wavelength.

During commissioning of the X-band receiver, a helical transmitter hooked up to a signal generator was used to directly illuminate the feed horns of the L- and S-band receivers with a field that was right-circularly polarized according to the IEEE convention. In both cases, the signal from the transmitter showed up only in the channels labeled left-circular polarization, which verified that the convention used, at least for these two receivers, is the optics convention. On the presumption that this was true for all other GBT receivers, it was determined that the labeling of the polarization channels for the X-band receiver should also follow this convention. Therefore, all figures, tables, and text in the memo do so as well.

7.2. Separation of right- and left-circular polarizations

In the X-band receiver, the single feed horn simultaneously supports both right- and left-circular polarization. Separation of the two polarizations into two channels is then accomplished by the combination of three waveguide elements: the phase shifter, 45 degree twist, and OMT (labeled in Figure 1 as W4, W5, and W6, respectively). The phase shifter, which consists of a (approximately) square waveguide with two sets of internal corrugations with differing widths, acts analogously to an optical 1/4-wave plate (Srikanth 1997): a linearly polarized wave whose electric field is aligned perpendicular to the phase shifter's fast axis experiences a 90 degree phase shift with respect to the wave polarized parallel to the fast axis (the orientation of the fast axis with respect to the two different sets of internal corrugations is shown in drawing 300002M091). Alternatively, if the wave

arriving at the phase shifter's input is circularly polarized, it becomes linearly polarized at the output and with the electric field oriented parallel to one of the diagonals of the square waveguide. For example, if the phase shifter is aligned for propagation along the $+z$-direction and its fast axis is aligned along the y-axis, a right-circularly polarized wave arriving at the input becomes the following at the phase shifter output:

$$\begin{aligned} \vec{E}_{R,out} =& (E_0/\sqrt{2})(i\vec{x} - i\vec{y}), \\ =& (iE_0/\sqrt{2})(\vec{x} - \vec{y}), \end{aligned} \tag{17}$$

where the complex exponential factor from Equation (16) has been dropped, as it does not affect the polarization direction.

The OMT is responsible for spatial separation of two linearly polarized modes propagating into its square cross-section input port, which arrive at either one of two rectangular, WR90 output ports. Optimal separation of these two modes into the two output ports (i.e. with minimal admixture) occurs when the both input waves are polarized parallel to either of the two sides of the square input port. The 45 degree twist, which is connected in between the phase shifter output and the OMT input, compensates for the above 45 degree rotation induced by the phase shifter. The net effect of these three is to separate right- and left-circularly polarized waves arriving at the phase shifter input into either of the two OMT outputs.

7.3. Cross-polarization

Perfect spatial separation of right- and left-circular polarizations as described above is not perfect: in general there is some cross-polarization between the X-band receiver's two output channels which effectively introduces some degree of ellipticity in the detected field. The total amount of cross-polarization which actually occurs in the receiver has not been measured, but an estimate can be made based on the known characteristics of a few of its components that are most likely to contribute.

The first likely contributor is the receiver feed horn in combination with the GBT reflector surfaces. An analysis of the polarization properties of the GBT including diffractive effects has been described in GBT Memo 102 (Srikanth 1993). In Figure 6 of the same memo, the cross-polarization as a function of the subreflector diameter and feed taper is plotted. As mentioned in Section 6, the edge taper for the X-band receiver is between 11 and 14 dB, while the subreflector diameter is 213 wavelengths across at 8 GHz. These parameters are off-scale in the figure, but it is assumed from the monotonic trend in the plot that the cross-polarization for this case is at most -40 dB.

We next consider the combination of the phase shifter, 45 degree twist, and OMT. As described in the preceding section, the phase shifter is designed to induce a 90 degree phase shift in one linear polarization with respect to the orthogonal one. In practice, however, this phase shift is found to deviate by up to 12 degrees within the range 8-12 GHz (see Figure 14). The net effect of this

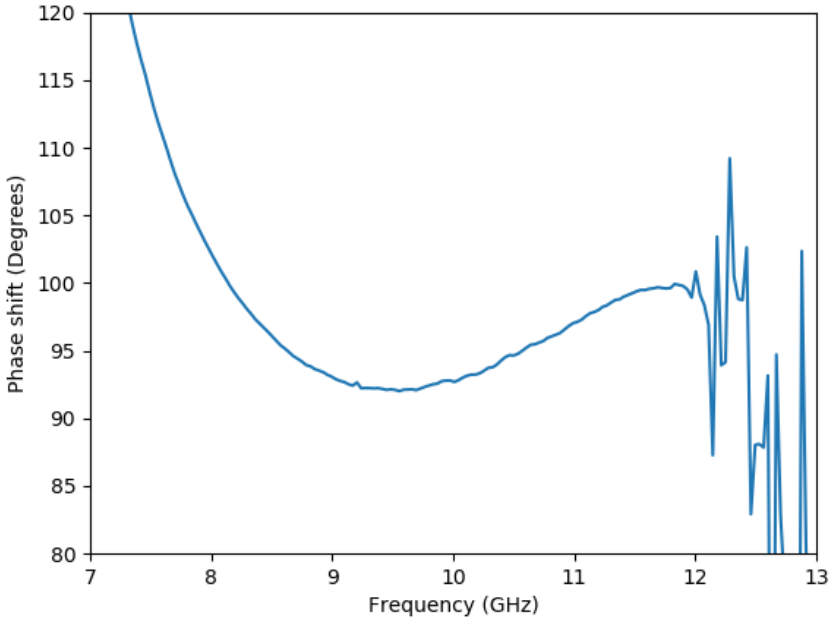

Fig. 14.— Measured differential phase shift between orthogonal linearly polarized modes of phase shifter

deviation to the combined cross-polarization of the phase shifter, 45 degree twist, and OMT has not been measured, but it can be estimated from the measured S-parameters of each of the individual components. The analysis is given in Appendix A, and the result is shown in Figure 15.

It can be seen from the figure that, within the range 8-12 GHz, the cross-polarization due to these three components is about -35 dB at best and -20 dB at worst. Note that from a comparison to Figure 14 it can be seen that the cross-polarization decreases as the phase shifter phase shift approaches 90°, as expected.

After the two circular polarizations have been spatially separated into two channels by the OMT, the corresponding signals later come into close physical proximity at two points in the receiver. The first of these is the transfer switch (SW3 in Figure 1). The transfer switch consists of a single X-Microwave block (part number XM-B8C6-0409D, see Section 11 for a general description of these blocks) with four RF traces routed to an RF DPDT switch (Qorvo CMD273P). The datasheet for the switch[2] specifies a channel isolation that varies between -40 dB at 8 GHz and -30 dB at 12 GHz. In this case, the isolated channels correspond to the left- and right-circular polarizations, so these values can be taken to be the associated cross-polarization due to the switch. Lab measurements

[2] https://www.qorvo.com/products/d/da007588

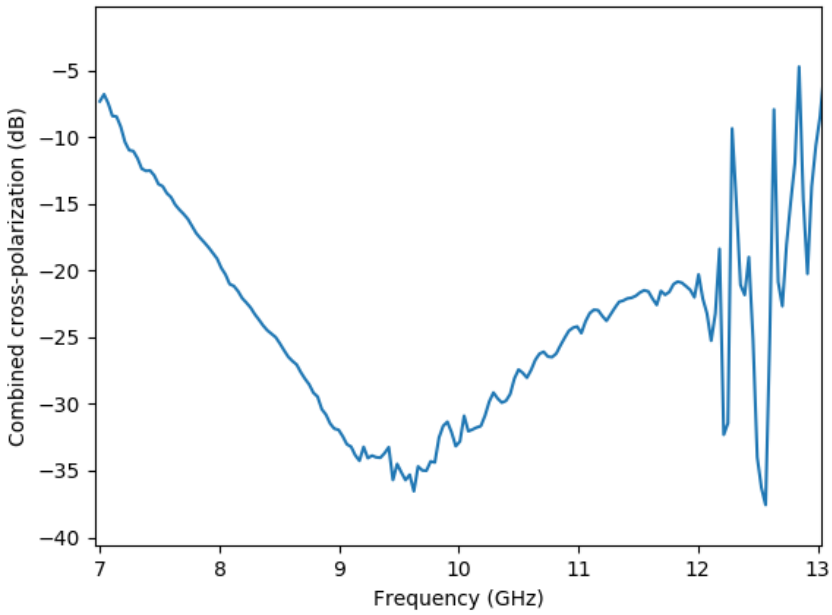

Fig. 15.— Combined cross-polarization due to phase shifter, 45 degree twist, and OMT

of the channel isolation including the PCB traces on the X-Microwave block show comparable or better values, indicating minimal coupling between traces.

The final location which may potentially contribute to the receiver's cross-polarization is at the branching point for the LO signal. The associated coupling path from the LCP channel to the RCP channel is shown in Figure 16. A signal that propagates along this path experiences attenuation predominantly due to the RF-LO and LO-IF isolation of the two mixers, the reverse isolation of the upper pair of amplifiers, the power divider output channel isolation, and the pair of attenuators AT4 and AT8. From the specifications of the associated devices, the net result is that the cross-polarization contribution from this coupling path is about -150 dB.

In summary then, cross-polarization in the receiver's RCP and LCP outputs may be present due to a number of components in the receiver and the GBT optical system, but the dominant contribution comes from the phase shifter, 45 degree twist, and OMT waveguide elements. The cross-polarization associated with these components varies from at best -35 dB at ∼9.5 GHz to at worst -20 dB elsewhere in the range 8-12 GHz.

8. Cryogenic low noise amplifiers

The receiver's first stage of amplification occurs with a pair of cryogenic LNAs linked thermally to the second stage of the receiver's refrigerator (at a nominal temperature of 15 K). Both consist of three cascaded InP pHEMT amplifiers (Diramics pH-100-2F100), each with its own independent

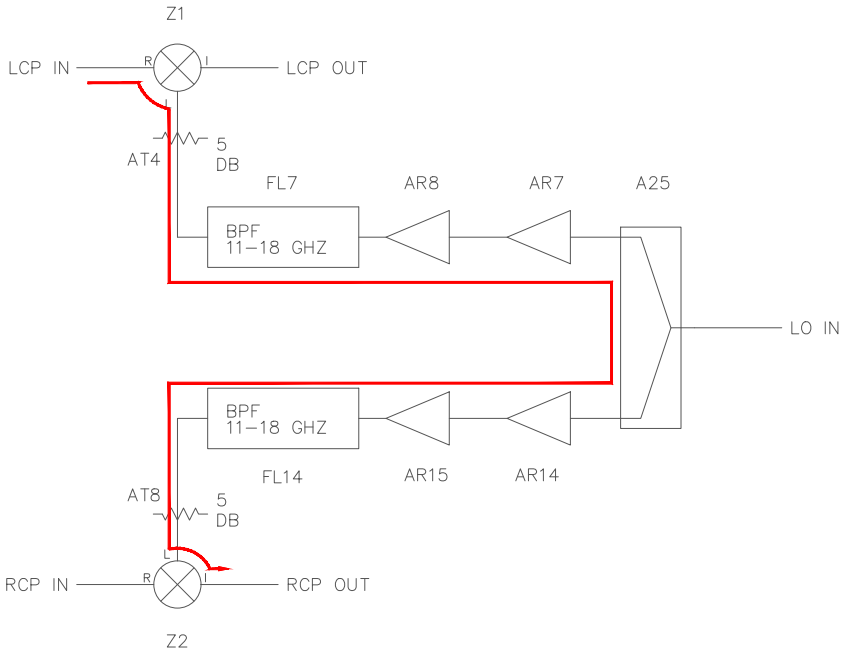

Fig. 16.— Potential coupling path between the two polarization channels in the X-band receiver downconverter module

bias network. Assembly of the chassis and biasing networks was carried out at the NRAO Central Development Laboratory (CDL). Drain and gate voltages to the bias network are supplied to each LNA by a standard NRAO Bias card (S1 and S2 in Figure 25), the output of which is limited by a diode limiter circuit before reaching the LNA bias inputs.

Biasing parameters were determined by CDL to optimize the noise temperature, and are shown in Table 4. The corresponding gain and noise temperature for both LNAs have been measured at 12 K by CDL, and are shown in Figure 17. The corresponding 1 dB output compression point has not been measured, but is estimated to be about -5 dBm. This can be increased with increased drain voltage and drain current to the third stage (up to about 1.7 V and 10 mA, respectively), but optimal parameters have not been determined. Both LNAs include LEDs, which, in the cryogenic LNAs for other GBT receivers, are illuminated in order to reduce hysteresis in the event that an amplifier becomes saturated. However, in the case of the X-band receiver's cryogenic LNAs, illuminating the LEDs was observed at CDL to increase the LNA noise temperature, and so the LEDs were left permanently disconnected.

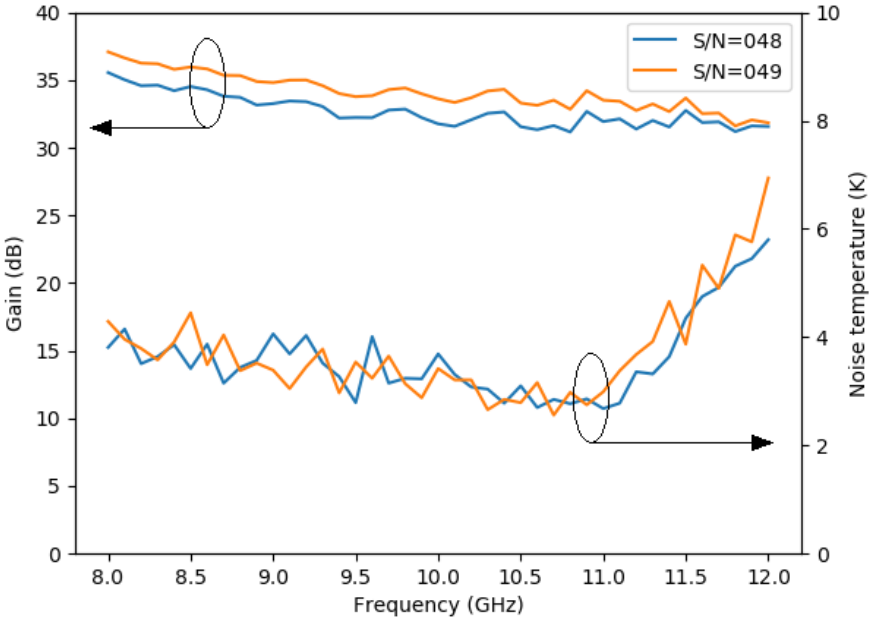

Fig. 17.— Gain and noise temperature for the X-band receiver's two cryogenic low noise amplifiers measured at T = 12.3 K.

9. Cryogenics

The upgraded X-band receiver is equipped with a CTI model 350 two-stage Gifford-McMahon refrigerator. Its first stage has a nominal unloaded base temperature of about 50 K and is thermally linked to a radiation shield and a clamp attached to the coaxial cables leading to the LNA outputs and the preceding couplers. The second stage has a nominal unloaded base temperature of 15 K and is thermally linked to the LNAs and waveguide components inside the receiver dewar and a charcoal cold trap. Under load due to radiative heating and conductive heating through the thermal transition, the first and second stages typically reach temperatures of 55 and 20 K, respectively.

Table 4. Biasing parameters for cryogenic amplifiers

Bias parameter	Stage 1	Stage 2	Stage 3
Drain Voltage (V)	0.77	0.8	0.8
Drain Current (mA)	4.25	2.70	2.50

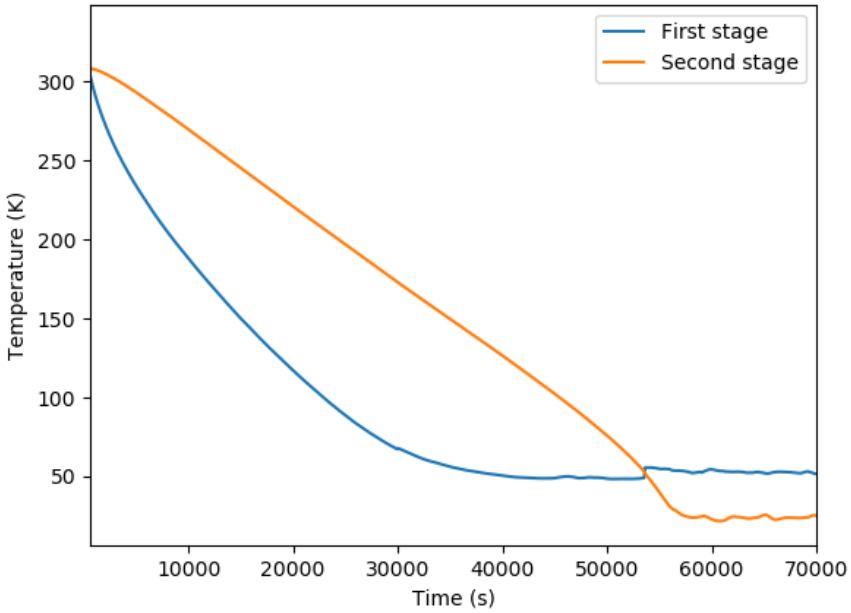

Fig. 18.— First and second stage refrigerator temperature during cool down from room temperature to base operational temperature

A cooldown plot from room temperature to loaded base temperature for both stages is shown in Figure 18. To both stages are affixed heaters which are connected in parallel to feedthrough connector J36, to which one may connect the output of a variac, for example, to power the heaters. Both heaters are in series with an independent thermostat to prevent overheating. A plot of the temperature of both stages as they warm up with applied heat from the heaters is shown in Figure 19. From these plots it can be seen that it takes approximately 16 hours for the receiver to cool down from room temperature and approximately 10 hours for it to warm up from its base operational temperatures.

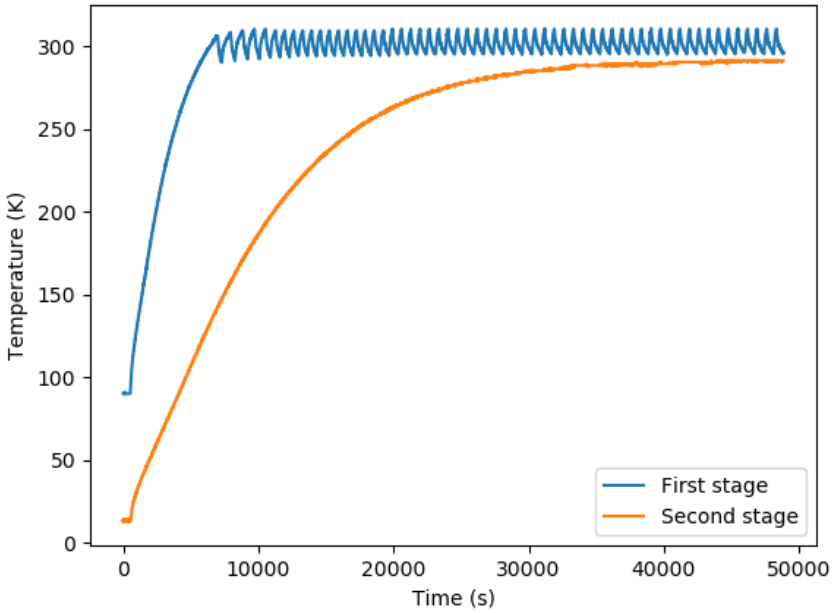

Fig. 19.— First and second stage refrigerator temperature during active warm up from base operational temperature to room temperature. The sawtooth pattern in first stage temperature is due to a thermostat attached to that stage cutting off power to the corresponding heater.

10. RFI considerations

In addition to the choice of IF center frequency (discussed in Section 5), another consequence of expanding the X-band receiver bandwidth to 8-12 GHz is that there is a higher likelihood for RFI, particularly with the recent proliferation of LEO satellite constellations such as those operated by SpaceX and OneWeb. In the US, Federal Communications Commission (FCC) frequency allocations exist for satellite communications between 10.7 and 12.7 GHz (FCC 2022), and both SpaceX and OneWeb have submitted and received approval for satellite constellations with downlinks in this range of frequencies (Weimer 2020; Wiltshire 2020).

Taking the May 2020 SpaceX FCC filing for its second generation Starlink constellation as an example, the expected power flux density at the earth's surface from Ku-band satellite emissions will be at most 244 MJy (see Table A.7-1 in Wiltshire 2020). Currently available information on the spectral structure of Starlink Ku-band downlinks show that the 10.7-12.7 GHz band is subdivided into 8 non-overlapping, 240 MHz wide channels (Humphreys et al. 2023). Assuming the main lobe of the GBT is directly illuminated by the main lobe of a Starlink satellite with only one channel active, this power flux density results in -25 dBm of total power at the input to the X-band receiver.

Table 5 shows the nominal power level of such a signal as it propagates through the receiver

(including lossy elements), and compares it at each stage to the 1 dB output compression level of the corresponding elements. In this case, only the second stage amplifier (RF amplifier 1, the first amplifier stage in the downconverter module) remains unsaturated. Notably, even the first, cryogenic stage of amplifiers would experience moderate saturation, whereas the final stage of IF amplifiers would be far overdriven, likely to the point of permanent damage (the power levels shown in the output column assume no saturation occurs, and are meant just to show the extent to which each device is overdriven).

Direct coupling between the main beam of the GBT and the main beam of any given Starlink satellite is expected to be exceedingly rare, as the satellites are currently programmed not to transmit within a small geographical region around the GBT.[3] Illumination of the GBT from a satellite sidelobe is still possible, and a preliminary study seems to suggest that the expected power flux density in this case is at most of the order 10 kJy (see Figure 9 of DePree et al. 2023). An analysis similar to that shown in Table 5 suggests this would result only in mild saturation of the final IF amplifier stage.

As of this writing, neither the SpaceX nor OneWeb satellite constellations have been fully deployed, and it remains to be seen what the exact frequency utilization and power flux densities will be once full deployment has been achieved. With this in mind, the X-band receiver has been equipped with the option to include notch filters for both the RCP and LCP channels (FL1 and FL8 in Figure 1) to protect the amplifiers and mixers in the downconverter module. Currently, switches are in place to either include or bypass the filters, but for the time being they have been permanently set in their "bypass" state and no notch filters have been installed, at least until more concrete information can be obtained about the expected downlink frequencies and associated power levels. Note: whatever filter ultimately is installed would, due to its location, offer no protection to the cryogenic amplifiers. But since these would only experience moderate saturation under worst-case conditions, it was determined that it would not be worth the effort and drawbacks associated with placing switches and filters inside the dewar for their protection (e.g. cost and increased receiver temperature).

[3] https://satellitemap.space/

Table 5. Direct coupling of a Starlink downlink into the GBT main beam is represented as -25 dBm of total power at the input to the X-band receiver and is shown at subsequent gain and mixing stages. Attenuation due to lossy components (not listed) is included, while amplifier saturation is ignored for the sake of showing the extent to which each element is overdriven. Component designators refer to Figure 1.

Component	Designator	Input power (dBm)	Output power (dBm)	P_{1dB} (dBm)
Cryogenic LNA	AR2/AR9	-25	10	-5
RF amplifier 1	AR3/AR10	4	19	28
RF amplifier 2	AR4/AR11	19	34	28
Mixer	Z1/Z2	27	15	6
IF amplifier 1	AR5/AR12	9	36	16
IF amplifier 2	AR6/AR13	36	63	16

11. X-Microwave Components

The X-band receiver's room temperature RF electronics, consisting of the transfer switch, down-converter module, and noise cal module are built around a prototyping platform developed by X-Microwave (now Quantic X-Microwave). The premise of the design is that each RF circuit element (e.g. amplifier, switch, mixer, etc.) is mounted to its own miniaturized RF circuit board called an X-Microwave block. Each block, in addition to the RF circuit element, includes 50 Ω grounded coplanar waveguide traces patterned onto the top layer to route signals from the edges of the block to the circuit element. A ground plane embedded 8 mils below the top layer forms the RF ground, which in turn is connected through vias to a ground plane on the bottom side of the block. Between the top layer and the embedded RF ground is a Rogers 4003 high frequency substrate.

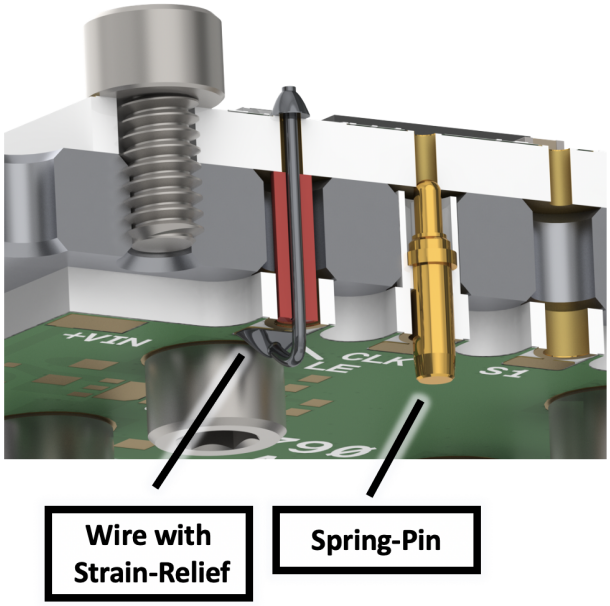

Fig. 20.— Cross-sectional view of an X-Microwave block, shown screwed onto the top of a breadboard. A bias and control board screwed to the bottom of the breadboard supplies biasing and/or control signals via a direct solder connection (left) or a solderless spring-pin connection fed through a hole in the breadboard to the bottom annulus of a via in the top X-Microwave block. The spring pin method is used exclusively for X-Microwave components in the X-band receiver. Image credit: Quantic X-Microwave.

RF signals can be routed between adjacent blocks by placing ground-signal-ground (GSG) jumpers over the gap between the blocks to provide electrical continuity between traces that meet at the block edges. Anchors screwed down on top of the GSG jumpers provide a compressive force to

maintain continuity without the use of a permanent solder connection. For prototyping applications, the blocks themselves are screwed down into a breadboard, which is made up of a 0.135" × 0.135" grid of threaded holes such that the blocks, which come in a small selection of form factors with clearance holes placed in standard locations, can be screwed down to the grid to form a complete RF circuit while still ensuring good alignment between adjacent traces.

All X-band receiver modules containing X-Microwave components are custom-designed enclosures that include a breadboard-like surface with an array of threaded holes, but that surface is in a recessed cavity which can only fit blocks of a certain form factor and bolt pattern. Nevertheless, blocks with the same form factor (and consequently often the same functionality, e.g. amplifier), can still be substituted for each other. This allows for easy replacement of defective blocks or upgrades.

Note: having the X-Microwave components inside of a recess risks having the coplanar waveguide modes couple into the cavity formed by the recess and the lid of the module. In this case, the width of these cavities is 0.54 inches, corresponding to an unloaded cutoff frequency of 10.9 GHz. Cavity modes have been observed during testing of the downconverter module, and have been suppressed through use of X-Microwave shields (part number: XM-SHIELD-01) and absorber adhered to the bottom side of the lid (Cuming Microwave C-RAM GDSS). This is further addressed in Section 14.1 on troubleshooting.

In order to route RF signals into and out of these modules, coaxial feedthroughs are used. These consist of an Anritsu "sparkplug" connector (part number K102F-R) and a sliding contact (part number K110-1-R) press-fit onto the connector's center pin and silver-epoxied to the signal trace of an X-Microwave block adjacent to the interior hole of the feedthrough.

Active devices such as amplifiers or switches receive power and control signals from "bias and control" blocks, which are mounted to the underside of the breadboard and connected to the corresponding RF blocks with spring pins, which pass through a hole at a given grid location in the breadboard and make contact with the annulus of a via on the bottom side of the RF block. As with the GSG jumpers, this forms a solderless connection which is maintained by the compressive force of the spring pin. A cross-sectional view of this arrangement is shown in Figure 20.

The bias and control blocks perform various functions depending on the associated RF component, including voltage regulation; reverse-polarity protection; level shifting; and, in the case of some amplifiers, active bias control for maintaining constant drain current. Power and control signals to the bias and control blocks themselves are established via direct connections to designated solder pads on those same blocks. Additional custom-designed blocks (e.g. inverter boards, signal distribution/fanout boards, etc.) with the same form factors and bolt patterns are also included in these layouts for various purposes. The layout of the X-Microwave blocks, both RF and bias and control, are shown for all modules in Figures 21 through 24. Further information about the

X-Microwave blocks and accessories can be obtained from the Quantic X-Microwave website.[4]

[4] https://quanticxmw.com/

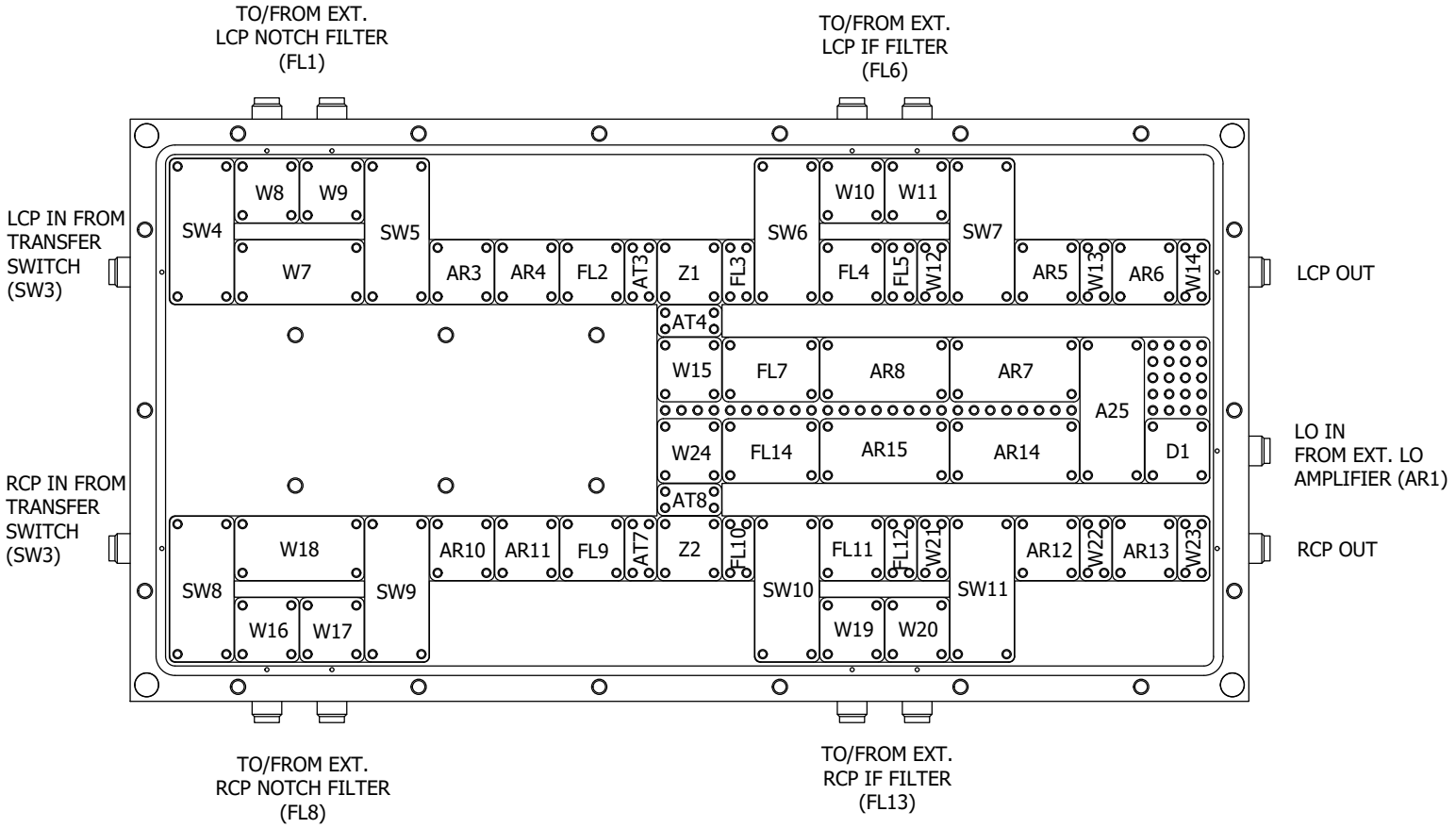

Fig. 21.— Layout of X-Microwave RF blocks in downconverter module. Designators refer to those in Figure 1. Part numbers, serial numbers, and core device information for each X-Microwave block are given in Table 6

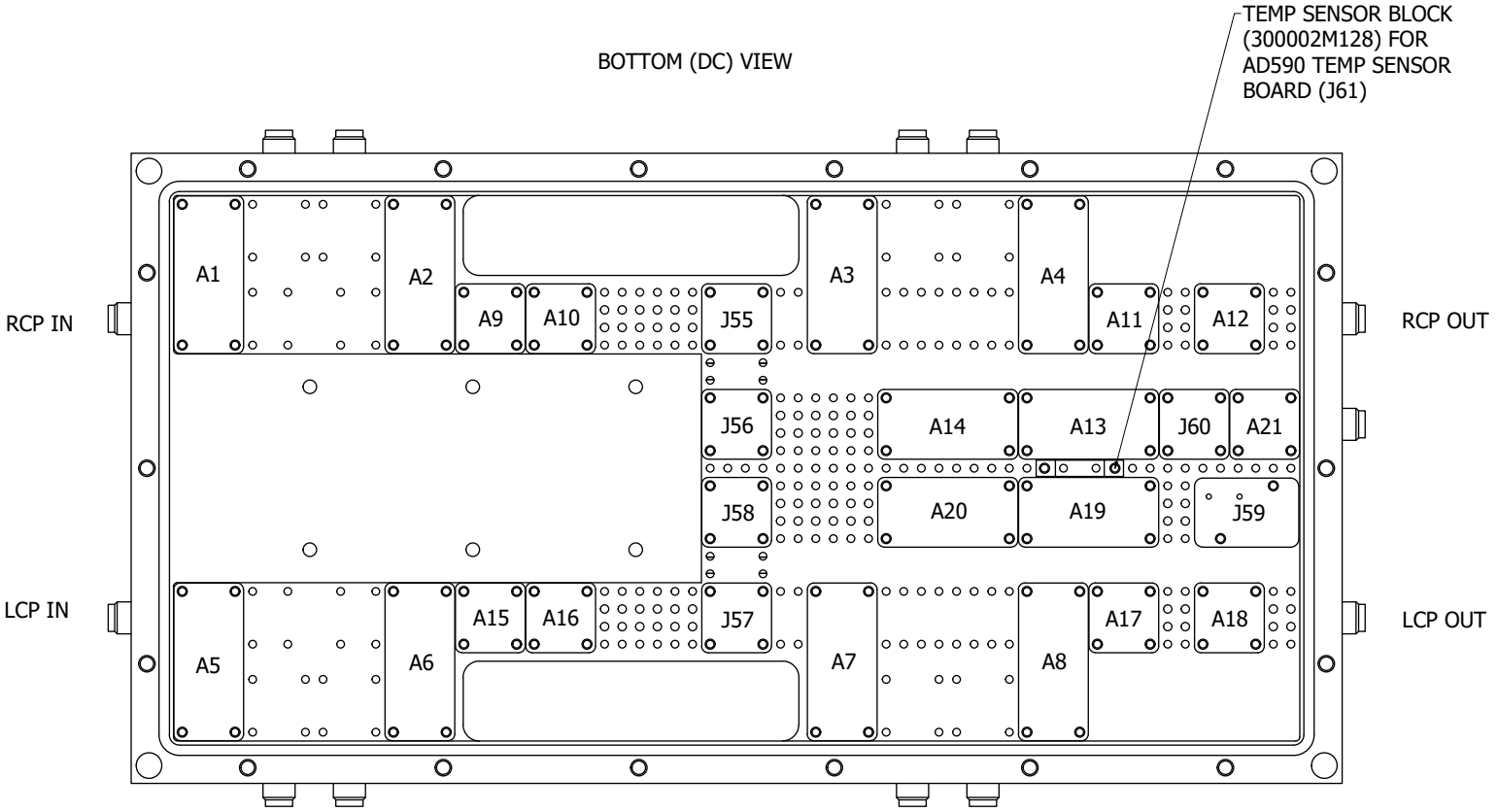

Fig. 22.— Layout of bias and control blocks in downconverter module. Designators refer to those in Figure 25. Part numbers, serial numbers, and biasing information are given in Table 7. Designators JXX refer to custom-designed circuit boards and are not included in the table (see Figure 25 for identification). Their circuit layouts and schematics are given in the drawings listed in Table 16 and 17.

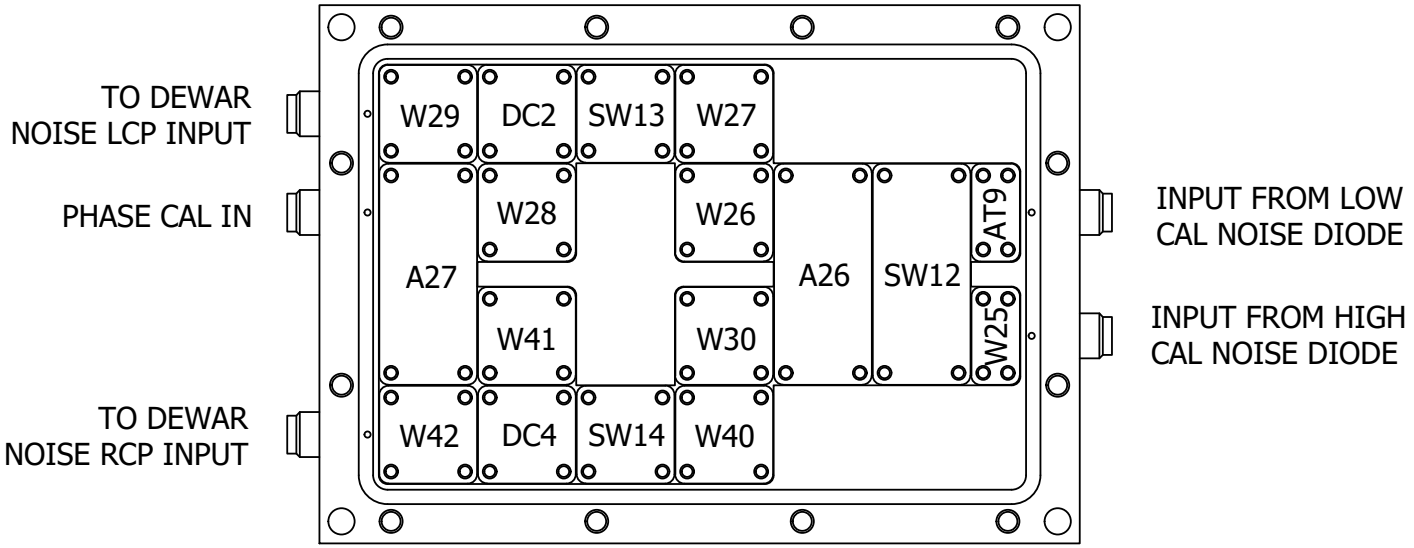

Fig. 23.— Layout of X-Microwave RF blocks in noise cal module. Designators refer to those in Figure 1. Part numbers, serial numbers, and core device information for each X-Microwave block are given in Table 8

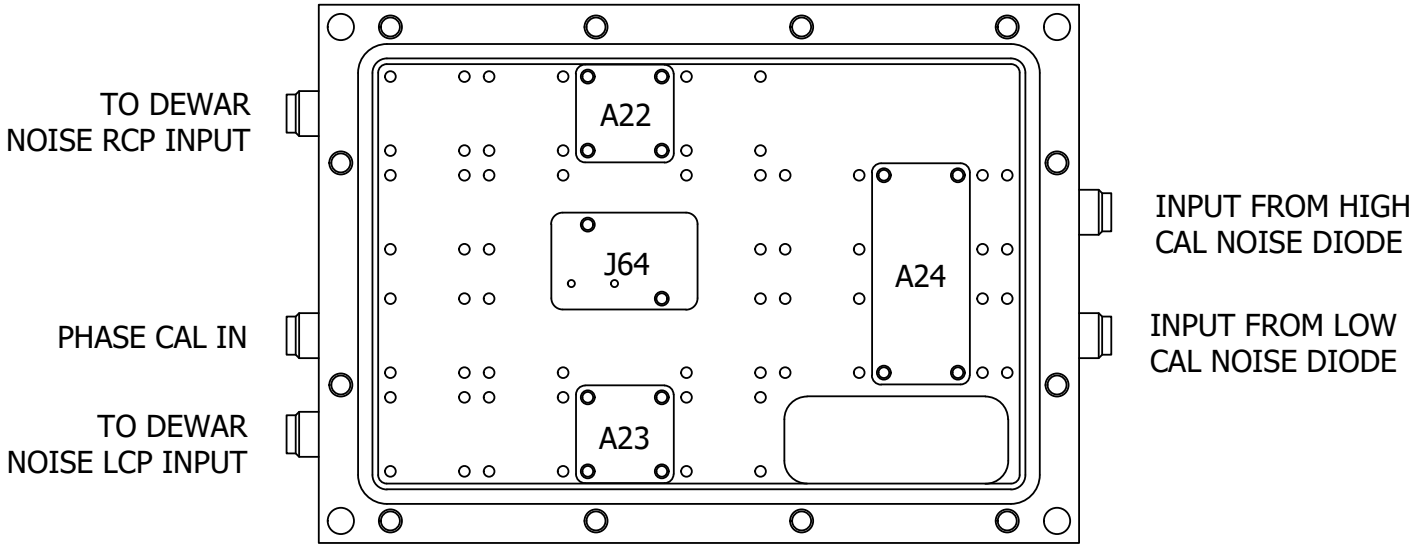

Fig. 24.— Layout of bias and control blocks in noise cal module. Designators refer to those in Figure 25. Part numbers, serial numbers, and biasing information are given in Table 9. Designator J64 refers to a custom-designed circuit board and is not included in the table (see Figure 25 for identification). Its circuit layout and schematic is given in the drawings listed in Table 16 and 17.

Table 6. X-Microwave RF blocks for X-band receiver downconverter module. Layout shown in Figure 21

Designator	Part no.	Serial no.	Description	Device mfr.	Mfr. part no.
SW4	XM-B6H9-0404D	27894	SPDT Switch	Analog	ADRF5024
W7	XM-A2M8-0404D	-	T-Line	-	-
W8	XM-A2M8-0404D	-	T-Line	-	-
W9	XM-A317-0804D	-	T-Line	-	-
SW5	XM-B1C9-0409D	27898	SPDT Switch	Analog	ADRF5024
AR3	XM-A9W5-0404D	27902	Amplifier	Qorvo	CMD278C4
AR4	XM-A9W5-0404D	27903	Amplifier	Qorvo	CMD278C4
FL2	XM-A2B3-0404D	27904	BP Filter	Knowles	B096QC2S
AT3	XM-A234-0204D	29828	Attenuator	Minicircuits	RCAT-05+
Z1	XM-B2D4-0404D	27906	Mixer	Marki	MM1-0626SSM
FL3	XM-A1H3-0204D	27907	LP Filter	Minicircuits	LFCN-8400+
SW6	XM-B6H9-0409D	27895	SPDT Switch	Analog	ADRF5024
W10	XM-A2M8-0404D	-	T-Line	-	-
W11	XM-A2M8-0404D	-	T-Line	-	-
SW7	XM-B1C9-0404D	27899	SPDT Switch	Analog	ADRF5024
FL4	XM-A9J9-0404D	27909	LP Filter	AVX	LP0AA6160A700
FL5	XM-A1D4-0204D	27911	HP Filter	Minicircuits	HFCN-1760+
W12	XM-A2M5-0204D	-	T-Line	-	-
AR5	XM-C7D7-0404D	64035	Amplifier	Qorvo	CMD295C4
W13	XM-A2M5-0204D	-	T-Line	-	-
AR6	XM-C7D7-0404D	64036	Amplifier	Qorvo	CMD295C4
W14	XM-A2M5-0204D	-	T-Line	-	-
AT4	XM-A234-0204D	29829	Attenuator	Minicircuits	RCAT-05+
W15	XM-A2M8-0404D	-	T-Line	-	-
FL7	XM-A265-0604D	27925	BP Filter	Knowles	B148QF0S
AR8	XM-A9R7-0804D	29819	Amplifier	Qorvo	CMD249P5
AR7	XM-A3E6-0804D	27927	Amplifier	Qorvo	CMD192C5
SW8	XM-B1C9-0409D	27900	SPDT Switch	Analog	ADRF5024
W16	XM-A2M8-0404D	-	T-Line	-	-
W17	XM-A2M8-0404D	-	T-Line	-	-
W18	XM-A317-0804D	-	T-Line	-	-
SW9	XM-B6H9-0409D	27896	SPDT Switch	Analog	ADRF5024
AR10	XM-A9W5-0404D	29823	Amplifier	Qorvo	CMD278C4

Table 6—Continued

Designator	Part no.	Serial no.	Description	Device mfr.	Mfr. part no.
AR11	XM-A9W5-0404D	29824	Amplifier	Qorvo	CMD278C4
FL9	XM-A2B3-0404D	27905	BP Filter	Knowles	B096QC2S
AT7	XM-A234-0204D	29830	Attenuator	Minicircuits	RCAT-05+
Z2	XM-B9G3-0404D	29827	Mixer	Marki	MM1-0626SSM
FL10	XM-A1H3-0204D	27908	LP Filter	Minicircuits	LFCN-8400+
SW10	XM-B1C9-0409D	27901	SPDT Switch	Analog	ADRF5024
W19	XM-A2M8-0404D	-	T-Line	-	-
W20	XM-A2M8-0404D	-	T-Line	-	-
SW11	XM-B6H9-0409D	27897	SPDT Switch	Analog	ADRF5024
FL11	XM-A9J9-0404D	27910	LP Filter	AVX	LP0AA6160A700
FL12	XM-A1D4-0204D	27912	HP Filter	Minicircuits	HFCN-1760+
W21	XM-A2M5-0204D	-	T-Line	-	-
AR12	XM-C7D7-0404D	64037	Amplifier	Qorvo	CMD295C4
W22	XM-A2M5-0204D	-	T-Line	-	-
AR13	XM-C7D7-0404D	64038	Amplifier	Qorvo	CMD295C4
W23	XM-A2M5-0204D	-	T-Line	-	-
AT8	XM-A234-0204D	29831	Attenuator	Minicircuits	RCAT-05+
W24	XM-A2M8-0404D	-	T-Line	-	-
FL14	XM-A265-0604D	27925	BP Filter	Knowles	B148QF0S
AR15	XM-A9R7-0804D	29820	Amplifier	Qorvo	CMD249P5
AR14	XM-A3E6-0804D	29834	Amplifier	Qorvo	CMD192C5
D1	XM-B7R4-0404D	29832	Detector	Macom	MACP-010573
A25	XM-A3R3-0409D	31962	Power Divider	Minicircuits	EP2K1+

Table 7. X-Microwave bias and control blocks for X-band receiver downconverter module. Layout shown in Figure 22

Designator	Part no.	Serial no.	Vin+ (V)	Vin- (V)	Ctl (V)
A1	XM-B1E2-0409D	27890	5	-15	0/3.3
A2	XM-B1E2-0409D	27891	5	-15	0/3.3
A3	XM-B1E2-0409D	27892	5	-15	0/3.3
A4	XM-B1E2-0409D	27893	5	-15	0/3.3
A5	XM-B1E2-0409D	27886	5	-15	0/3.3
A6	XM-B1E2-0409D	27887	5	-15	0/3.3
A7	XM-B1E2-0409D	27888	5	-15	0/3.3
A8	XM-B1E2-0409D	27889	5	-15	0/3.3
A9	XM-B127-0404D	29825	12.5	-	-
A10	XM-B127-0404D	29826	12.5	-	-
A11	XM-A5C8-0404D	64041	12	-	-
A12	XM-A5C8-0404D	64042	12	-	-
A13	XM-A379-0804D	29835	12	-	-
A14	XM-B936-0804D	29822	12.5	-	-
A15	XM-B127-0404D	27928	12.5	-	-
A16	XM-B127-0404D	27929	12.5	-	-
A17	XM-A5C8-0404D	64039	12	-	-
A18	XM-A5C8-0404D	64040	12	-	-
A19	XM-A379-0804D	27926	12	-	-
A20	XM-B936-0804D	29821	12.5	-	-
A21	XM-C7R4-0404D	29833	15	-	-

Table 8. X-Microwave RF blocks for X-band receiver noise cal module. Layout shown in Figure 23

Designator	Part no.	Serial no.	Description	Device mfr.	Mfr. part no.
AT9	XM-B4Y2-0204D	31967	Attenuator	Minicircuits	KAT-10+
SW12	XM-B6H9-0409D	31965	SPDT Switch	Analog	ADRF5024
A26	XM-A3R3-0409D	31964	Power Divider	Minicircuits	EP2K1+
W26	XM-A2M8-0404D	-	T-Line	-	-
W27	XM-A2M8-0404D	-	T-Line	-	-
SW13	XM-A5A8-0404D	31958	SPST Switch	Qorvo	CMD204C3
DC2	XM-A2Y3-0404D	31957	Coupler	Knowles	FPC06074
W29	XM-A2M7-0404D	-	T-Line	-	-
W28	XM-A2M8-0404D	-	T-Line	-	-
A27	XM-A3R3-0409D	31963	Power Divider	Minicircuits	EP2K1+
W25	XM-A2M5-0204D	-	T-Line	-	-
W30	XM-A2M8-0404D	-	T-Line	-	-
W40	XM-A2M8-0404D	-	T-Line	-	-
SW14	XM-A5A8-0404D	31959	SPST Switch	Qorvo	CMD204C3
DC4	XM-B9Y3-0404D	31968	Coupler	Knowles	FPC06074
W42	XM-A2M7-0404D	-	T-Line	-	-
W41	XM-A2M8-0404D	-	T-Line	-	-

Table 9. X-Microwave bias and control blocks for X-band receiver noise cal module. Layout shown in Figure 24

Designator	Part no.	Serial no.	Vin+ (V)	Vin- (V)	Ctl (V)
A22	XM-A5A9-0404D	31961	-	-15	0/3.3
A23	XM-A5A9-0404D	31960	-	-15	0/3.3
A24	XM-B1E2-0409D	31965	5	-15	0/3.3

12. Monitor and Control

In addition to the RF electronics represented in the block diagram in Figure 1, various supporting electronics are also included for monitor and control functions, as shown in Figure 25. Monitored analog voltages include those relating to the receiver's DC power supply; cryogenics; and the biasing of the LNAs, noise diodes, and downconverter module amplifiers. Monitored digital voltages include the states of the external CAL and SIG/REF signals as well as the actual states of the cal and transfer switches. Available control functions include enabling or disabling the biasing of LNAs or noise diodes and the toggling of various switches in the downconverter or noise cal modules (e.g. IF filter select switches and the switch selecting either the high cal or low cal noise diode).

The core monitor and control processing unit for the receiver consists of a LAN-connected Odroid-N2 single board computer, which in turn is connected via USB to a Numato 64 channel general purpose input/output (GPIO) board. The Odroid-N2 runs a Linux-based operating system which contains two files (the configuration file `/home/odroid/python/config/xband.conf` and the monitor points file `/home/odroid/python/monitor_points/XBR_v1p12.csv`) which specify, among other things, the Odroid-N2 IP address, the GPIO board configuration, and various information about the monitor and control signals (e.g. GPIO pin mappings, available sample rates, etc.). On bootup, the Odroid-N2 runs an installed software package called the GBO Receiver Interface Module for Electronics (GRIME), which handles commands from the instrument user (through the receiver's software manager) and converts the raw voltages monitored by the GPIO board into the corresponding quantities expressed in physical units, which are then streamed back to the user. For each monitored quantity, the details of this conversion depend on the output conditioning circuitry for the associated sensor, the details of which are given in sections 12.1 through 12.4. Section 12.5 describes the receiver's remote reset feature, which allows the instrument user to remotely power cycle the Odroid-N2 in the event that it is unresponsive or otherwise malfunctioning.

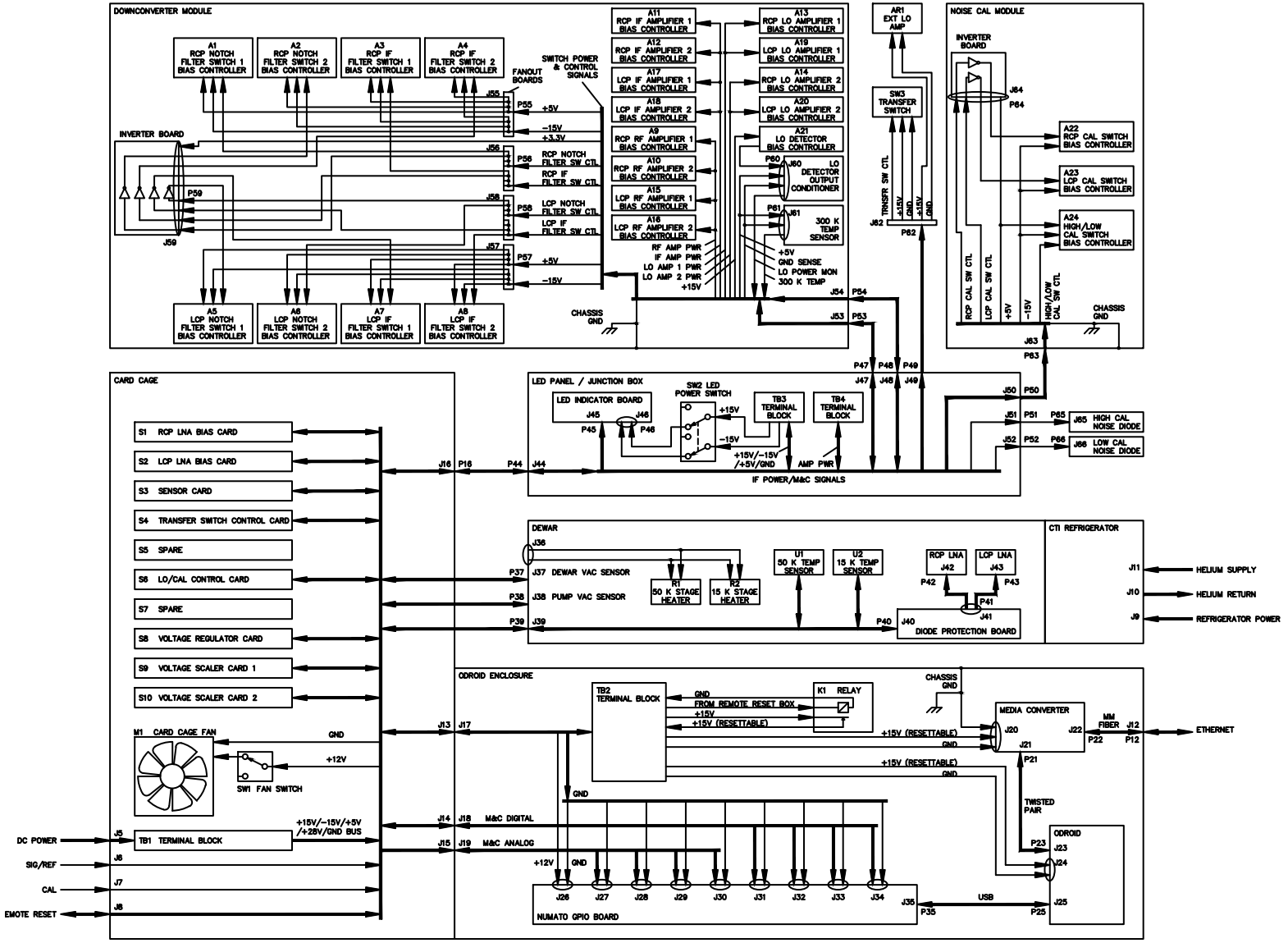

Fig. 25.— Block diagram for the X-band receiver's power distribution and monitor and control electronics

12.1. LO power monitor

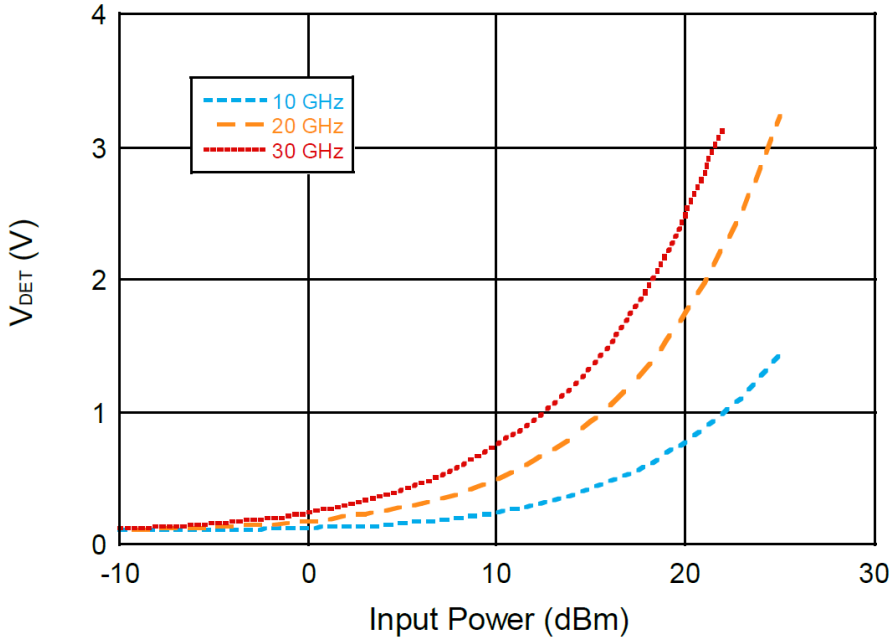

Fig. 26.— Response of LO power detector (MACOM MACP-010573) versus LO frequency and power. Figure taken from MACP-010573 datasheet.[5]

At the LO input of the downconverter module is an X-Microwave detector block (XM-B7R4-0404D) for detecting the LO power. The core device of this block is a MACOM MACP-010573 temperature-compensated directional power detector with a nominal bandwidth of 10-30 GHz (the nominal LO frequency range for the X-band receiver is 11-19 GHz). The detector's output voltage is a nonlinear function of both the power and frequency of its input, as shown in Figure 26. It has been assumed that this functional relationship has the form:

$$V_{det} = V_0 + \kappa P^{\gamma} f^{\delta}, \tag{18}$$

where V_0 is a DC offset in Volts, κ is a constant coefficient, P is the input power in mW, f is the frequency in GHz, and γ and δ are the corresponding constant exponents. By injecting a tone with known frequency and power into the LO input of the downconverter and measuring the detector output voltage, the constants in (18) were determined to be:

$$\begin{aligned} V_0 &= 0.0946 \\ \kappa &= 0.0011327 \\ \gamma &= 0.6272 \\ \delta &= 1.5316 \end{aligned} \tag{19}$$

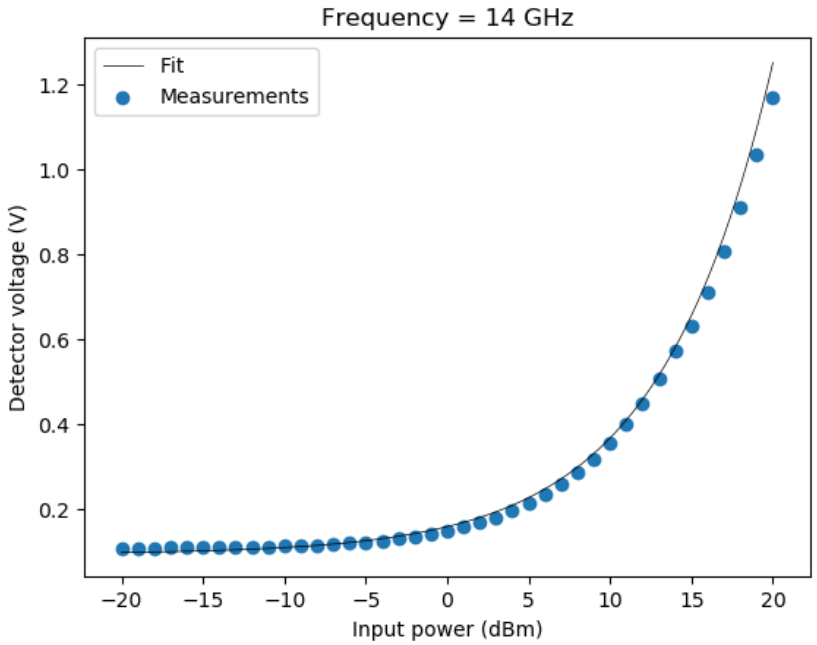

Fig. 27.— Measured response of LO power detector for an injected tone of varying power and fixed frequency $f = 14$ GHz. Line shows Equation (18) with parameters given in Equation (19).

A representative plot showing the agreement between the measured data with the fit is shown in Figure 27.

In order to determine the input power from the known detector voltage and LO frequency, one must invert Equation (18):

$$P = \left(\frac{V - V_0}{\kappa f^{\delta}} \right)^{1/\gamma} \tag{20}$$

Because this conversion requires knowledge of the LO frequency, which is not accessible to the GRIME service on the Odroid-N2, it is performed by the X-band software manager, which knows the hard-coded parameters given in Equation (19) and is simultaneously subscribed to the IF Manager, which in turn knows the LO frequency (either `LO1A_frequency` or `LO1B_frequency` depending on the chosen configuration). Once the LO power level in mW has been calculated according to Equation (20), one final step is performed to linearly re-scale the value as follows:

$$P' = \frac{5P}{P_0}, \tag{21}$$

where P_0 is equal to 1 mW or 0 dBm, the nominal input power level to the downconverter module.

[5] https://cdn.macom.com/datasheets/MACP-010573.pdf

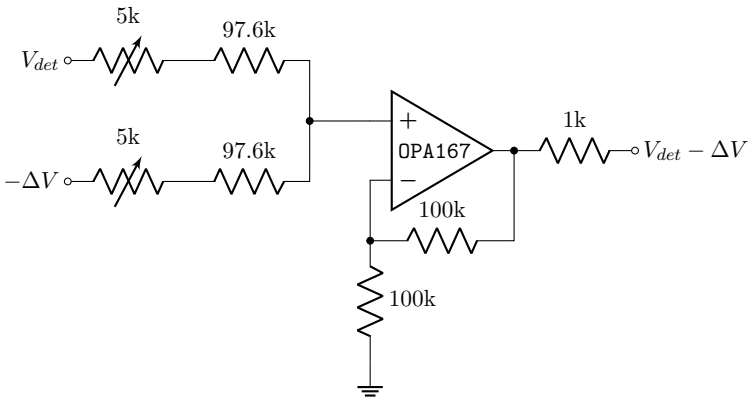

Fig. 28.— Simplified circuit schematic for LO power detector output conditioner

Equation (21) effectively maps P_0 to a value of 5, which historically has been the nominal "target level" for the LO power of other GBT receivers.

It is worth pointing out that there are some sources of error in the reported LO power level. The first has to do with the accuracy of the fitting equation (18). With the detector placed at the LO input to the downconverter module as shown in Figure 1, it will be expected to detect a nominal power level of 0 dBm under normal operating conditions. Figure 27 shows that for this power level, the input power level inferred from the fit will be underestimated, but only by a few dB. Note also that, due to small measurement error, it is possible that the measured detector voltage may fall below the minimum voltage V_0 implied by the fit (18). In this case, the LO power reported by the X-band software manager will be clipped to zero irrespective of frequency.

One final source of error is due to the difference in ground potential ΔV between the LO power detector and the Numato GPIO board, where the detector voltage is ultimately digitized and stored. The result of this is that the GPIO board measures $V_{det} + \Delta V$ instead of the actual detector voltage V_{det}. It has been found in practice that ΔV may be of the order of a few hundred mV, which is comparable to typical values for V_{det}, and so it is important to correct for this offset. To do so, the output conditioner circuit shown in Figure 28 was placed between the LO power detector and the GPIO board. The circuit is a simple summing amplifier with unity gain and is located just adjacent to the LO power detector (such that they share the same ground potential). One input is connected directly to the LO power detector output, whereas the other is connected to the ground nearest to the GPIO board, which, with respect to the ground local to the conditioner circuit, is just $-\Delta V$, precisely cancelling the offset that would have appeared at the GPIO board. Note, 5 kΩ trimpots are placed at the inputs to compensate for incomplete cancellation due to resistor tolerances.

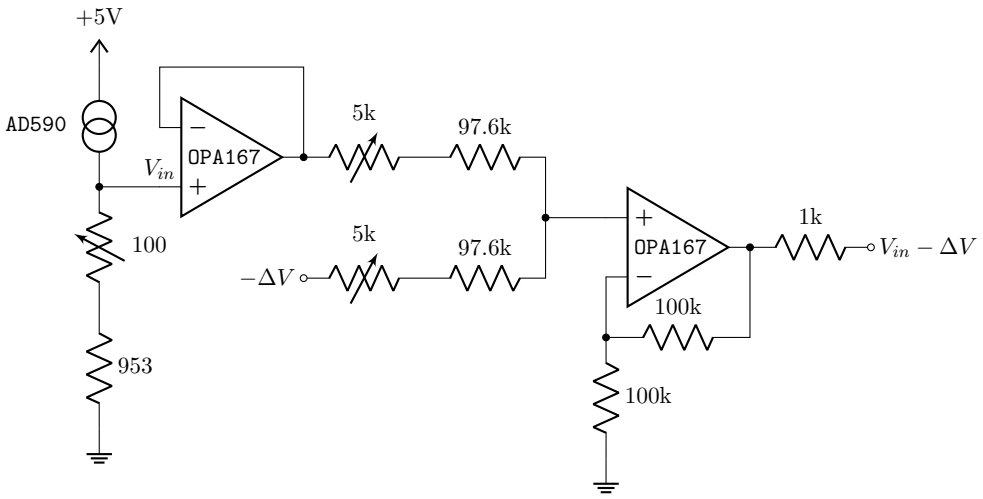

Fig. 29.— Simplified circuit schematic for AD590 temperature sensor output conditioner

12.2. 300 K temperature monitor

The 300 K temperature sensor measures the temperature of the X-band receiver's downconverter module. The module is nominally at room temperature, although due to the many RF amplifiers and associated voltage regulators housed inside of it, it can reach temperatures of approximately 50 °C or higher. It is not currently equipped with any form of active cooling, but X-band software manager does raise a warning when the temperature exceeds 100 °C.

The temperature sensor itself consists of an Analog Devices AD590 in direct thermal contact with the downconverter module chassis. Biasing and output conditioning of the AD590 is done as shown in Figure 29. As described in the datasheet for the AD590[6], it sources an output current of approximately 1 μA per Kelvin. The input V_{in} to the first op-amp is therefore nominally equal to 1 mV·K^{-1} times the absolute temperature, which is in turn buffered at the output of the same op-amp (the 100 Ω trimpot allows for slight adjustment of the temperature-to-voltage scaling factor). From here, the voltage is fed into an identical circuit to the output conditioner for the LO power detector (see Section 12.1), and so any offset ΔV between the downconverter module and the GPIO board is automatically compensated. Conversion from voltage back to temperature in Kelvins is performed by GRIME.

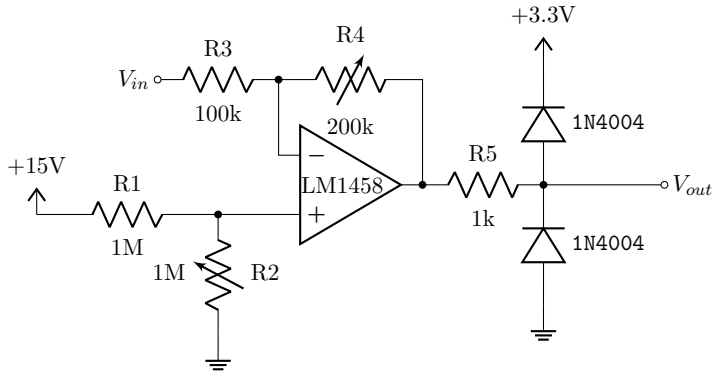

Fig. 30.— Simplified circuit schematic for the analog voltage scaling subcircuit of the voltage scaling card

12.3. Voltage scaling cards

The Numato 64 channel GPIO board used for monitoring and controlling the X-band receiver hardware is specified to have TTL compatible GPIO pins with a nominal operating voltage between 0 and 3.3 V and a maximum current sink/source capacity of 20 mA. Therefore, to allow it to be safely interfaced with the receiver hardware, two voltage scaling cards (S9 and S10 in Figure 25) were built. Each of these cards features a set of inverting op-amp subcircuits used to scale up to 12 analog voltages to within the 0 to 3.3 V range of the GPIO inputs, one Texas Instruments CD4050B non-inverting hex buffer for logic level shifting from CMOS devices (0 to 5 V), and one OnSemi NUD3124LT1G inductive load driver to allow the GPIO pins to control relays (in particular, the Schneider W171DIP-14 relays used on the LNA bias cards for switching on and off the drain voltage).

A simplified schematic for one of the inverting amplifier subcircuits is shown in Figure 30. The transfer function for the subcircuit may be expressed as:

$$\begin{aligned} V_{out} &= -A(V_{in} - V_0), \\ A &= R_4/R_3, \\ V_0 &= \frac{R_2}{R_1 + R_2} V_b, \end{aligned} \tag{22}$$

where $V_b = 15$ V. This is just a linear transformation of the input voltage with slope $-A$ and intercept AV_0, either of which may be adjusted (though not independently) by the trimpots R2 and R4 in order to map a range of voltages expected at the input into the range 0 to 3.3 V which is compatible with the GPIO board. Note, the combination of R5 and the pair of diodes at the output of the op amp clip the output to nominally -0.7 V to 4.0 V for additional protection of the

[6] https://www.analog.com/media/en/technical-documentation/data-sheets/AD590.pdf

GPIO board while still maintaining acceptable linearity in the transfer function given by Equation (22). To obtain the un-scaled V_{in}, one applies the inverse of Equation (22) to the measured V_{out}:

$$V_{in} = -(1/A)V_{out} + V_0. \tag{23}$$

This step is performed by GRIME, for which the slope $A' = -(1/A)$ and intercept V_0 is specified for each analog monitor point in the multipliers and offsets columns of the monitor points spreadsheet stored on the Odroid-N2. If the voltage V_{in} is the output of a sensor, an additional rescaling may be reflected in the multiplier and offset which also converts V_{in} to the sensed quantity (e.g. pressure or temperature). Note: any adjustment to the trimpots R2 and R4 in the subcircuit shown in Figure 30 will therefore require a corresponding change to the multiplier and offset for that monitor point.

12.4. Voltage regulator card

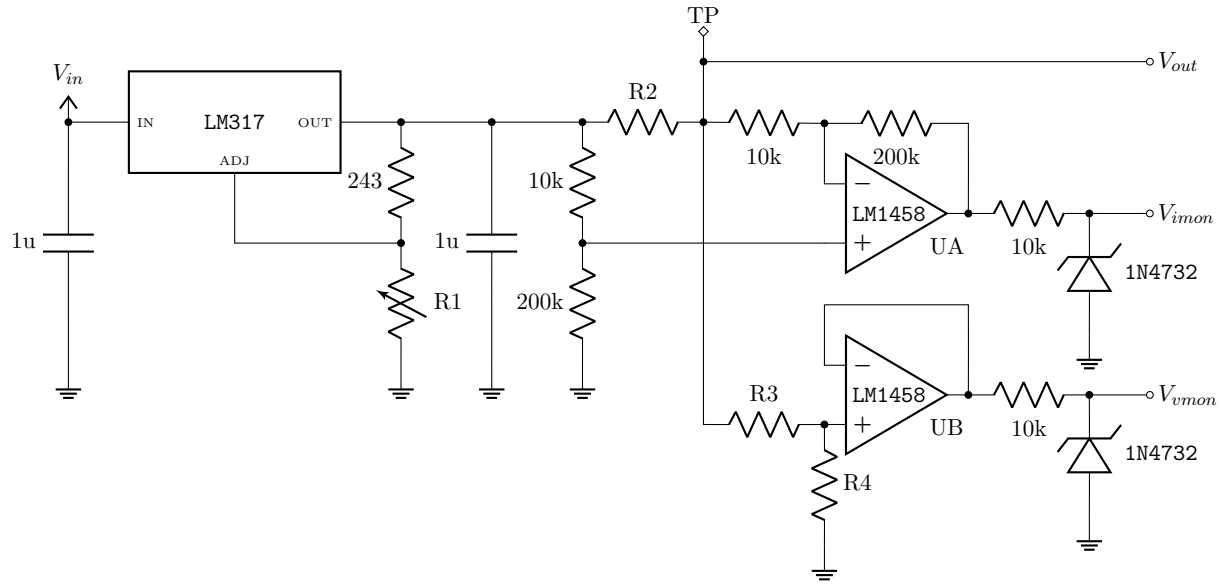

Fig. 31.— Subcircuit for positive, regulated output voltage from voltage regulator card

The bias controllers which regulate the supply voltage to the amplifiers in the downconverter module have recommended input voltages that range between 5 and 11 V depending upon the corresponding amplifier. In order to accommodate this range of voltages, a voltage regulator card was designed and built (S8 in Figure 25). The card features 10 adjustable voltage regulators supplied with either 15 V, -15 V, or 5 V, which in turn may be regulated down to the range 1.25 to 13 V, -13 to -1.25 V, or 1.25 to 3.3 V, respectively. Six of the adjustable outputs may be tuned within the first range, while only two are available that can be tuned within each of the latter two ranges (see Table 10). The subcircuit corresponding to positive output voltages is shown in Figure 31 and the subcircuit corresponding to negative output voltages is shown in Figure 32.

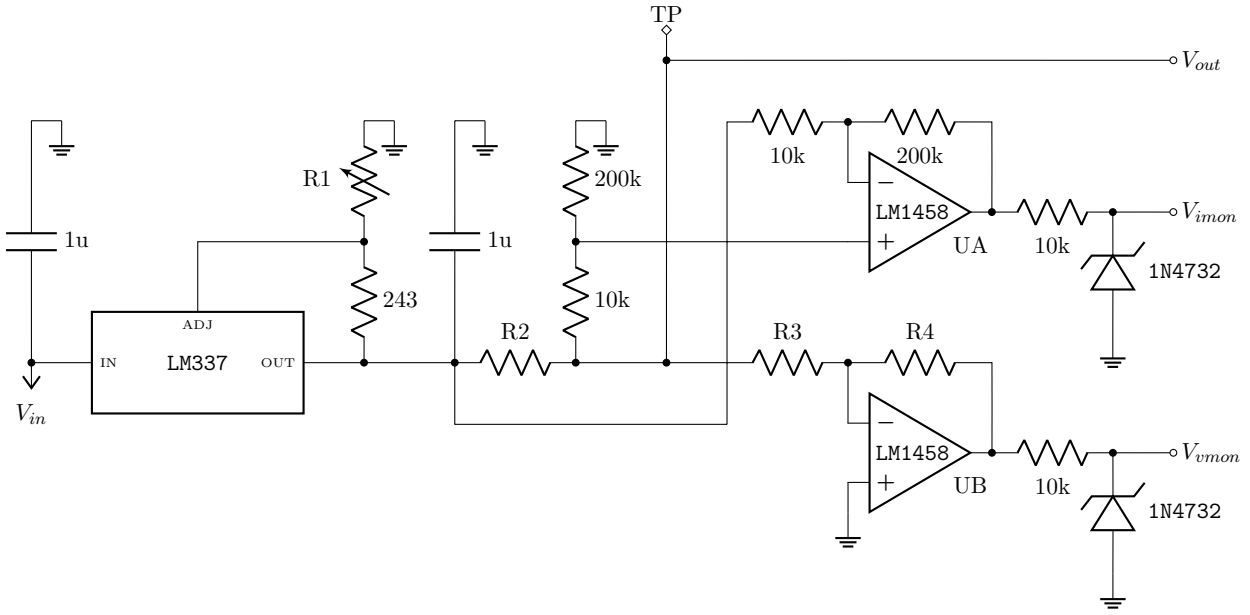

Fig. 32.— Subcircuit for negative, regulated output voltage from voltage regulator card

For both subcircuits, the trimpot R1 allows tuning of the output voltage, and its full-scale resistance is chosen such that the tunable range encompasses those given above (which are limited by the voltage regulators). For each output, the card has a test point (labeled TP) that may be probed with a voltmeter. Additionally, it includes two further outputs, V_{imon} and V_{vmon}, which, respectively, monitor the output current and voltage. V_{imon} and V_{vmon} may be expressed for both the positive and negative output subcircuits as:

$$V_{imon} = AI_{out}, \tag{24}$$

$$V_{vmon} = A'V_{out}, \tag{25}$$

where the sign of the output current I_{out} is defined to be positive for current flowing left to right through resistor R2 and the numerical values of the coefficients A and A' are given in Table 10. For the positive output subcircuit:

$$\begin{aligned} A =& 20R_2, \\ A' =& \frac{R_4}{R_3 + R_4}, \end{aligned} \tag{26}$$

whereas for the negative output subcircuit:

$$\begin{aligned} A =& -20R_2, \\ A' =& -\frac{R_4}{R_3}. \end{aligned} \tag{27}$$

Under normal operating conditions, V_{imon} and V_{vmon} are positive for all subcircuits, and resistors R2, R3, and R4 are chosen such that they remain within the range 0 to 3.3 V so that they can be

directly routed to the Numato GPIO board. Additional protection to the GPIO board is afforded by the use of the 10 kΩ output resistors and 1N4732 Zener diodes, which limit V_{imon} and V_{vmon} to nominally -0.7 to 4.0 V while maintaining reasonable linearity within the range of the GPIO inputs. Inversion of Equations (24) and (25) to obtain the actual output voltage and current is accomplished by GRIME as described in Section 12.3 for the voltage scaler card.

Currently, for a few of the regulated outputs, the current draw is close to or exceeding 1 A, which requires a few Watts of heat dissipation for the voltage regulator in question. To prevent the voltage regulators from going into thermal shutdown, each was mounted to the PCB with a heatsink, with the associated contact area populated by several thermal vias to the bottom ground plane for the purpose of heat spreading. Under these conditions, the regulators were still found to intermittently go into thermal shutdown, and so a fan was installed on the receiver's card cage to allow forced air cooling, which eliminated the problem. Further discussion is included in Section 14.1.

Table 10: Voltage regulator card configuration for each of its 10 outputs. See Equations (24) and (25) for definitions of A and A'.

#	V_{in} (V)	V_{out} range (V)	V_{out} (V)	A (V/A)	A' (V/V)	Function
1	+15	+1.25 to +13	+12.0	2.0	0.13	IF Amplifier Bias
2	+15	+1.25 to +13	+12.5	2.0	0.13	LO Amplifier 2 Bias
3	+15	+1.25 to +13	+12.0	2.0	0.13	LO Amplifier 1 Bias
4	+15	+1.25 to +13	+12.5	2.0	0.13	RF Amplifier Bias
5	+15	+1.25 to +13	+12.0	2.0	0.13	Numato Board Power
6	+15	+1.25 to +13	+12.0	2.0	0.13	Card Cage Fan Power
7	-15	-1.25 to -13	-	-2.0	-0.14	Spare
8	-15	-1.25 to -13	-	-2.0	-0.14	Spare
9	+5	+1.25 to +3.5	+3.3	200	0.39	Inverter Board Power
10	+5	+1.25 to +3.5	-	200	0.39	Spare

12.5. Remote reset

In the event that the Odroid becomes unresponsive, accommodation has been made to remotely reset it by means of the remote reset box in the GBT receiver room. This is accomplished by routing power to the Odroid as shown in Figure 33. Under normal operating conditions, the relay inside the reset box is de-energized, which in turn leaves the receiver's relay K1 de-energized. In this case, the Odroid and media converter both receive power from the +15 V supply through the normally closed (NC) contacts of relay K1.

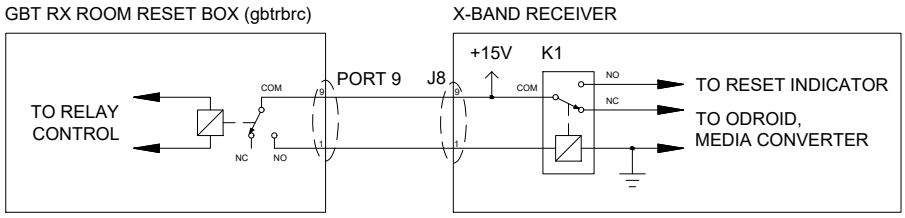

Fig. 33.— Simplified block diagram showing connections between X-band receiver and the GBT receiver room's reset box (hostname: gbtrbrc)

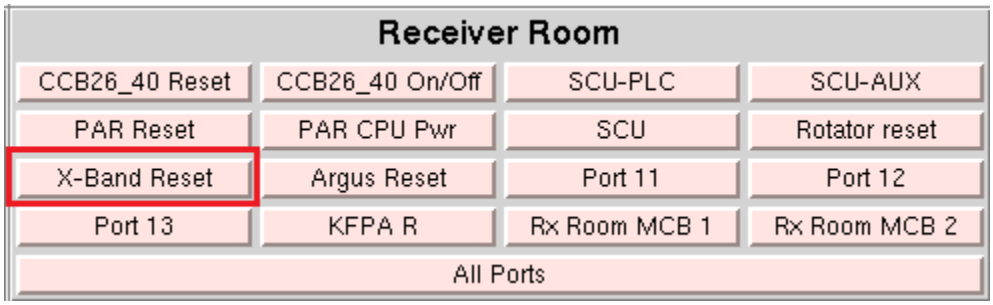

Fig. 34.— Receiver room panel of reset box Cleo window showing button for resetting X-band receiver highlighted in red box. Pressing this button resets the receiver's Odroid and media converter by removing power for 5 seconds.

When the reset box's relay is energized, this in turn energizes K1, switching power from the Odroid and media converter to a remote reset LED indicator on the receiver's front panel. Currently, the reset box is configured to remove power to the Odroid and media converter for a duration of 5 seconds (as found in the configuration file `/home/gbt/etc/config/ResetBox.conf`), after which point both relays are de-energized and power is restored to both the Odroid and media converter. To initiate a remote reset, one presses the "X-Band Reset" button in the Reset Box Cleo window (see Figure 34). Note: all other components in the X-band receiver, including the Numato GPIO board remain powered on throughout the reset period.

13. Drawings List

Table 11: Assembly drawings

Dwg. no.	Dwg. date	Dwg. title	Frmt.
300002A001	7/29/2021	Frame Assembly	ACAD
300002A002	11/12/2021	Odroid Tray	ACAD
300002A003	7/28/2021	RF Plate Assembly	ACAD
300002A004	6/8/2022	Slide Assembly	ACAD
300002A005	1/20/2022	Odroid Enclosure	ACAD
300002A006	4/27/2021	Card Cage	ACAD
300002A007	11/15/2021	Card Cage Cable Conduit	ACAD
300002A008	7/21/2021	Junction Box	ACAD
300002A009	3/5/2021	Downconverter Module	ACAD
300002A010	4/9/2021	Noise Cal Module	ACAD
300002A011	4/13/2021	Transfer Switch	ACAD
300002A012	8/8/2021	Turret Hole Cover Assembly	ACAD
300002A013	8/9/2021	Defroster Stand	ACAD
300002A014	8/7/2021	Feed Support	ACAD
300002A015	2/11/2021	Feed Horn Assembly	ACAD
300002A016	3/19/2020	Thermal Transition	ACAD
300002A017	6/22/2022	OMT Support V2 Assembly	ACAD
300002A018	6/22/2022	Waveguide Assembly	ACAD
300002A019	6/23/2022	Cold Shield	ACAD
300002A020	8/31/2021	15 K Stage Assembly	ACAD
300002A021	2/17/2021	Cal Kit, 0.900 Square to 0.947 Square Adapter	ACAD
300002A022	6/23/2022	Feed Horn Test Setup	ACAD
300002A023	6/24/0222	Thermal Transition Test Setup	ACAD
300002A024	6/23/2022	Circular to Square Transition Test Setup	ACAD
300002A025	6/24/2022	Phase Shifter Test Setup	ACAD
300002A026	6/24/2022	45 Degree Twist Test Setup	ACAD
300002A027	6/24/2022	OMT Test Setup	ACAD
300002A028	7/3/2023	Card Cage Fan Plate Assembly	ACAD
300002A029	11/27/2022	Downconverter Module X-Microwave Block Layout	ACAD
300002A030	11/12/2023	Noise Cal Module X-Microwave Block Layout	ACAD

Table 12. Bills of materials

Dwg. no.	Dwg. date	Dwg. title	Frmt.
300002B001	6/1/2020	Voltage Scaling Board BOM	Excel
300002B002	4/16/2021	Voltage Regulator Board BOM	Excel
300002B003	11/13/2023	Led Indicator Board BOM	Excel
300002B004	11/13/2023	Fanout Board BOM	Excel
300002B005	3/17/2022	Inverter Board BOM	Excel
300002B006	12/9/2022	AD590 Temp Sensor Output Board BOM	Excel
300002B007	3/17/2022	LO Power Detector Output Board BOM	Excel
300002B008	6/2/2021	Transfer Switch Bias Board BOM	Excel

Table 13. Data documents

Dwg. no.	Dwg. date	Dwg. title	Frmt.
300002D001	9/6/2019	Feed Horn Inner Radius Profile	Excel
300002D002	6/11/2021	Feed Horn S11	S1P
300002D003	7/8/2021	Feed Horn Farfield Msrmt., E-Plane, Co-Pol, Y=-13	LST
300002D004	7/8/2021	Feed Horn Farfield Msrmt., E-Plane, Co-Pol, Y=-12	LST
300002D005	7/8/2021	Feed Horn Farfield Msrmt., E-Plane, Co-Pol, Y=-11	LST
300002D006	7/6/2021	Feed Horn Farfield Msrmt., E-Plane, Co-Pol, Y=-10	LST
300002D007	7/6/2021	Feed Horn Farfield Msrmt., E-Plane, Co-Pol, Y=-9	LST
300002D008	7/6/2021	Feed Horn Farfield Msrmt., E-Plane, Co-Pol, Y=-8	LST
300002D009	7/6/2021	Feed Horn Farfield Msrmt., E-Plane, Co-Pol, Y=-7	LST
300002D010	7/6/2021	Feed Horn Farfield Msrmt., E-Plane, Co-Pol, Y=-6	LST
300002D011	7/6/2021	Feed Horn Farfield Msrmt., E-Plane, Co-Pol, Y=-5	LST
300002D012	7/6/2021	Feed Horn Farfield Msrmt., E-Plane, Co-Pol, Y=-4	LST
300002D013	7/6/2021	Feed Horn Farfield Msrmt., E-Plane, Co-Pol, Y=-3	LST
300002D014	7/6/2021	Feed Horn Farfield Msrmt., E-Plane, Co-Pol, Y=-2	LST
300002D015	7/6/2021	Feed Horn Farfield Msrmt., E-Plane, Co-Pol, Y=-1	LST
300002D016	7/6/2021	Feed Horn Farfield Msrmt., E-Plane, Co-Pol, Y=0	LST
300002D017	7/6/2021	Feed Horn Farfield Msrmt., E-Plane, Co-Pol, Y=1	LST
300002D018	7/6/2021	Feed Horn Farfield Msrmt., E-Plane, Co-Pol, Y=2	LST
300002D019	7/6/2021	Feed Horn Farfield Msrmt., E-Plane, Co-Pol, Y=3	LST
300002D020	7/6/2021	Feed Horn Farfield Msrmt., E-Plane, Co-Pol, Y=4	LST
300002D021	7/6/2021	Feed Horn Farfield Msrmt., E-Plane, Co-Pol, Y=5	LST
300002D022	7/9/2021	Feed Horn Farfield Msrmt., H-Plane, Co-Pol, Y=-13	LST
300002D023	7/9/2021	Feed Horn Farfield Msrmt., H-Plane, Co-Pol, Y=-12	LST
300002D024	7/9/2021	Feed Horn Farfield Msrmt., H-Plane, Co-Pol, Y=-11	LST
300002D025	6/30/2021	Feed Horn Farfield Msrmt., H-Plane, Co-Pol, Y=-10	LST
300002D026	6/30/2021	Feed Horn Farfield Msrmt., H-Plane, Co-Pol, Y=-9	LST
300002D027	6/30/2021	Feed Horn Farfield Msrmt., H-Plane, Co-Pol, Y=-8	LST
300002D028	6/30/2021	Feed Horn Farfield Msrmt., H-Plane, Co-Pol, Y=-7	LST
300002D029	6/30/2021	Feed Horn Farfield Msrmt., H-Plane, Co-Pol, Y=-6	LST
300002D030	6/30/2021	Feed Horn Farfield Msrmt., H-Plane, Co-Pol, Y=-5	LST
300002D031	6/30/2021	Feed Horn Farfield Msrmt., H-Plane, Co-Pol, Y=-4	LST
300002D032	6/30/2021	Feed Horn Farfield Msrmt., H-Plane, Co-Pol, Y=-3	LST
300002D033	6/30/2021	Feed Horn Farfield Msrmt., H-Plane, Co-Pol, Y=-2	LST

Table 13—Continued

Dwg. no.	Dwg. date	Dwg. title	Frmt.
300002D034	6/30/2021	Feed Horn Farfield Msrmt., H-Plane, Co-Pol, Y=-1	LST
300002D035	6/30/2021	Feed Horn Farfield Msrmt., H-Plane, Co-Pol, Y=0	LST
300002D036	6/30/2021	Feed Horn Farfield Msrmt., H-Plane, Co-Pol, Y=1	LST
300002D037	6/30/2021	Feed Horn Farfield Msrmt., H-Plane, Co-Pol, Y=2	LST
300002D038	6/30/2021	Feed Horn Farfield Msrmt., H-Plane, Co-Pol, Y=3	LST
300002D039	6/30/2021	Feed Horn Farfield Msrmt., H-Plane, Co-Pol, Y=4	LST
300002D040	6/30/2021	Feed Horn Farfield Msrmt., H-Plane, Co-Pol, Y=5	LST
300002D041	7/9/2021	Feed Horn Farfield Msrmt., E-Plane, Co-Pol, Y=-12.392	LST
300002D042	7/9/2021	Feed Horn Farfield Msrmt., E-Plane, Co-Pol, Y=-10.837	LST
300002D043	7/8/2021	Feed Horn Farfield Msrmt., E-Plane, Co-Pol, Y=-9.516	LST
300002D044	7/9/2021	Feed Horn Farfield Msrmt., E-Plane, Co-Pol, Y=-8.481	LST
300002D045	7/8/2021	Feed Horn Farfield Msrmt., E-Plane, Co-Pol, Y=-7.576	LST
300002D046	7/9/2021	Feed Horn Farfield Msrmt., E-Plane, X-Pol, Y=-12.397	LST
300002D047	7/9/2021	Feed Horn Farfield Msrmt., E-Plane, X-Pol, Y=-10.837	LST
300002D048	7/9/2021	Feed Horn Farfield Msrmt., E-Plane, X-Pol, Y=-8.481	LST
300002D049	7/9/2021	Feed Horn Farfield Msrmt., H-Plane, Co-Pol, Y=-12.392	LST
300002D050	7/9/2021	Feed Horn Farfield Msrmt., H-Plane, Co-Pol, Y=-10.837	LST
300002D051	7/9/2021	Feed Horn Farfield Msrmt., H-Plane, Co-Pol, Y=-8.481	LST
300002D052	7/9/2021	Feed Horn Farfield Msrmt., H-Plane, X-Pol, Y=-12.392	LST
300002D053	7/9/2021	Feed Horn Farfield Msrmt., H-Plane, X-Pol, Y=-10.837	LST
300002D054	7/9/2021	Feed Horn Farfield Msrmt., H-Plane, X-Pol, Y=-8.481	LST
300002D055	7/9/2021	Feed Horn Farfield Msrmt., D-Plane, X-Pol, Y=-12.392	LST
300002D056	7/9/2021	Feed Horn Farfield Msrmt., D-Plane, X-Pol, Y=-10.837	LST
300002D057	7/9/2021	Feed Horn Farfield Msrmt., D-Plane, X-Pol, Y=-8.481	LST
300002D058	7/9/2021	Feed Horn Phase Efficiency Calculation	Zip
300002D059	10/14/2022	Thermal Transition S Parameters	Chx
300002D060	5/10/2021	Circular To Square Transition, Rect. Port Cal.	Chx
300002D061	5/10/2021	Circular To Square Transition, Cir. Port Cal.	S2P
300002D062	5/10/2021	Circular To Square Transition S/N 001 S Params	S2P
300002D063	5/10/2021	Circular To Square Transition S/N 002 S Params	S2P
300002D064	4/5/2021	Phase Shifter X-Pol To X-Pol S Params	S2P
300002D065	4/5/2021	Phase Shifter Y-Pol To Y-Pol S Params	S2P
300002D066	4/5/2021	Phase Shifter Differential Phase Shift Calculation	Zip

Table 13—Continued

Dwg. no.	Dwg. date	Dwg. title	Frmt.
300002D067	3/26/2021	45 Degree Twist 0.900 Square Port Calibration	Chx
300002D068	3/26/2021	45 Degree Twist 0.947 Square Port Calibration	Chx
300002D069	3/26/2021	45 Degree Twist S Parameters	S2P
300002D070	10/14/2022	OMT S-Parameters, X-Pol Input Port, Port 3 Terminated	S2P
300002D071	10/14/2022	OMT S Params, X-Pol Input Port, Port 2 Terminated	S2P
300002D072	10/14/2022	OMT S Params, X-Pol Input Port, Input Port Terminated	S2P
300002D073	10/14/2022	OMT S-Parameters, Y-Pol Input Port, Port 3 Terminated	S2P
300002D074	10/14/2022	OMT S Params, Y-Pol Input Port, Port 2 Terminated	S2P
300002D075	10/14/2022	OMT S Params, Y-Pol Input Port, Input Port Terminated	S2P
300002D076	6/18/2020	Cross-Guide Coupler S/N J506062770 S Params, CPL-IN	S2P
300002D077	6/18/2020	Cross-Guide Coupler S/N J506062770 S Params, CPL-OUT	S2P
300002D078	6/18/2020	Cross-Guide Coupler S/N J506062770 S Params, IN-OUT	S2P
300002D079	6/18/2020	Cross-Guide Coupler S/N J506062771 S Params, CPL-IN	S2P
300002D080	6/18/2020	Cross-Guide Coupler S/N J506062771 S Params, CPL-OUT	S2P
300002D081	6/18/2020	Cross-Guide Coupler S/N J506062771 S Params, IN-OUT	S2P
300002D082	1/21/2020	Waveguide Isolator S/N 105 (Spare) S Params	S2P
300002D083	1/21/2020	Waveguide Isolator S/N 106 S Params	S2P
300002D084	1/21/2020	Waveguide Isolator S/N 107 S Params	S2P
300002D085	5/17/2021	Cryo Lna S/N 048 S Paramss, T=15 K	S2P
300002D086	5/11/2021	Cryo Lna S/N 049 S Paramss, T=15 K	S2P
300002D089	9/1/2023	Monitor And Control Specifications	Excel

Table 14. Block diagrams

Dwg. no.	Dwg. date	Dwg. title	Frmt.
300002K001	11/3/2023	RF Block Diagram	ACAD
300002K002	11/3/2023	Power and Monitor and Control Block Diagram	ACAD

Table 15. Mechanical drawings

Dwg. no.	Dwg. date	Dwg. title	Frmt.
300002M001	7/29/2021	Left Front Rail	ACAD
300002M002	7/29/2021	Right Front Rail	ACAD
300002M003	7/29/2021	Left Back Rail	ACAD
300002M004	7/29/2021	Right Back Rail	ACAD
300002M005	7/29/2021	Bottom Rail	ACAD
300002M006	11/12/2021	Odroid Tray Bottom Plate	ACAD
300002M007	11/12/2021	Odroid Tray L-Bracket	ACAD
300002M008	11/12/2021	Odroid Tray Right Side Plate	ACAD
300002M009	11/12/2021	Odroid Tray Left Side Plate	ACAD
300002M010	11/12/2021	Odroid Tray Pin Hole Support	ACAD
300002M011	11/12/2021	Odroid Tray Pin Hole	ACAD
300002M012	7/28/2021	RF Plate	ACAD
300002M013	7/28/2021	RF Plate, Noise Diode Divider	ACAD
300002M014	7/28/2021	RF Plate, Noise Diode Cover Plate	ACAD
300002M015	7/28/2021	RF Plate, Downconverter Corner Support	ACAD
300002M016	7/28/2021	RF Plate, Noise Cal Corner Support	ACAD
300002M017	7/28/2021	RF Plate, Large L-Bracket	ACAD
300002M018	7/28/2021	RF Plate, Medium L-Bracket	ACAD
300002M019	7/28/2021	RF Plate, Small L-Bracket	ACAD
300002M020	7/28/2021	RF Plate, Cable Tray	ACAD
300002M021	7/28/2021	RF Plate, Sma Connector Plate	ACAD
300002M022	5/19/2021	Slide Outer Lock Pin Attachment	ACAD
300002M023	5/19/2021	Slide Lock Pin Spacer	ACAD
300002M024	1/20/2021	Odroid Enclosure, Bottom Plate	ACAD
300002M025	1/20/2021	Odroid Enclosure, Side Walls	ACAD
300002M026	1/20/2021	Odroid Enclosure, Top Plate	ACAD
300002M027	1/20/2021	Odroid Enclousre, Odroid Shield	ACAD
300002M028	3/3/2021	Odroid Enclosure, Waveguide Below Cutoff	ACAD
300002M029	5/14/2021	Odroid Enclosure, Card Cage Spacer	ACAD
300002M030	4/27/2021	Card Cage, Top Plate	ACAD
300002M031	4/27/2021	Card Cage, Connector End Plate	ACAD
300002M032	4/27/2021	Card Cage, End Plate	ACAD
300002M033	4/27/2021	Card Cage, Bottom Plate	ACAD

Table 15—Continued

Dwg. no.	Dwg. date	Dwg. title	Frmt.
300002M034	4/28/2021	Card Cage, Edge Card Connector Plate	ACAD
300002M035	11/15/2021	Card Cage Conduit, Connector Plate	ACAD
300002M036	11/15/2021	Card Cage Conduit, Side Plate	ACAD
300002M037	11/15/2021	Card Cage Conduit, Back Plate	ACAD
300002M038	11/15/2021	Card Cage Conduit, Top Plate	ACAD
300002M039	7/21/2021	Junction Box, Connector Plate	ACAD
300002M040	7/21/2021	Junction Box, Blank Plate	ACAD
300002M041	7/21/2021	Junction Box, Led Plate	ACAD
300002M042	7/21/2021	Junction Box, Top Plate	ACAD
300002M043	7/21/2021	Junction Box, Bottom Plate	ACAD
300002M044	3/5/2021	Downconverter Module, Breadboard	ACAD
300002M045	3/5/2021	Downconverter Module, Top/Bottom Lid	ACAD
300002M046	4/9/2021	Noise Cal Module, Breadboard	ACAD
300002M047	4/9/2021	Noise Cal Module, Lid	ACAD
300002M048	4/13/2021	Transfer Switch, Breadboard	ACAD
300002M049	4/13/2021	Transfer Switch, Lid	ACAD
300002M050	9/10/2021	RF Plate, Transfer Switch Power Tab	ACAD
300002M051	2/27/2020	RF Feedthru Mounting Plate	ACAD
300002M052	6/10/2022	DC Hermetic Feedthru Plate	ACAD
300002M053	6/10/2022	AC Hermetic Feedthru Plate	ACAD
300002M054	2/28/2020	KF-40 Half Nipple Mounting Plate	ACAD
300002M055	2/27/2020	Refrigerator Standoff	ACAD
300002M056	3/23/2020	Dewar Bottom Plate	ACAD
300002M057	2/27/2020	Dewar Cylinder	ACAD
300002M058	3/20/2020	Dewar Top Plate	ACAD
300002M059	8/8/2021	Turret Hole Cover Assembly, Turret Hole Cover	ACAD
300002M060	8/8/2021	Turret Hole Cover Assembly, Vertical Strut	ACAD
300002M061	8/8/2021	Turret Hole Cover Assembly, Angle Strut	ACAD
300002M062	8/9/2021	Defroster Stand, Foot	ACAD
300002M063	8/9/2021	Defroster Stand, Fixed Tube	ACAD
300002M064	8/9/2021	Defroster Stand, Sliding Tube	ACAD
300002M065	8/9/2021	Defroster Stand, Weld Tab	ACAD
300002M066	8/7/2021	Feed Support, Ring 1	ACAD

Table 15—Continued

Dwg. no.	Dwg. date	Dwg. title	Frmt.
300002M067	8/7/2021	Feed Support, Ring 2	ACAD
300002M068	8/7/2021	Feed Support, Ring 3	ACAD
300002M069	8/7/2021	Feed Support, Ring 4	ACAD
300002M070	8/7/2021	Feed Support, Flex Plate	ACAD
300002M071	8/7/2021	Feed Support, Cylinder	ACAD
300002M072	2/11/2021	Feed Horn, Section 1	ACAD
300002M073	2/11/2021	Feed Horn, Section 2	ACAD
300002M074	2/11/2021	Feed Horn, Section 3	ACAD
300002M075	2/11/2021	Feed Horn, Ring Corrugation Tube	ACAD
300002M076	2/11/2021	Feed Horn, Ring Loaded Corrugations	ACAD
300002M077	2/11/2021	Feed Horn, Throat	ACAD
300002M078	2/11/2021	Feed Horn, Throat Extension	ACAD
300002M079	8/9/2021	Feed Horn, Radome Ring	ACAD
300002M080	2/15/2021	Thermal Transition, Iris	ACAD
300002M081	3/20/2020	Thermal Transition, Upper Waveguide	ACAD
300002M082	2/17/2021	Thermal Transition, Foam Plug	ACAD
300002M083	3/20/2020	Thermal Transition, Long G10 Rod	ACAD
300002M084	4/13/2022	Thermal Transition, Bottom Plate	ACAD
300002M085	4/13/2022	Thermal Transition, Short G10 Rod	ACAD
300002M086	3/19/2020	Thermal Transition, Lower Waveguide	ACAD
300002M087	11/13/2019	Circular To Square Transition Mandrel	ACAD
300002M088	11/11/2019	Circular To Square Transition	ACAD
300002M089	11/8/2019	Phase Shifter Mandrel	ACAD
300002M090	6/4/2020	Phase Shifter	ACAD
300002M091	6/17/2022	Phase Shifter, Note On Polarization	ACAD
300002M092	11/7/2019	45 Degree Twist Mandrel	ACAD
300002M093	11/12/2019	45 Degree Twist	ACAD
300002M094	8/24/2021	OMT Support V2, Alignment Pin	ACAD
300002M095	8/31/2021	OMT Support V2, Alignment Pin Catch	ACAD
300002M096	8/24/2021	OMT Support V2, Bottom Plate	ACAD
300002M097	8/24/2021	OMT Support V2, Top Plate	ACAD
300002M098	1/21/2021	OMT Modifications	ACAD
300002M099	2/28/2020	Cold Shield, Bottom Plate	ACAD

Table 15—Continued

Dwg. no.	Dwg. date	Dwg. title	Frmt.
300002M100	2/28/2020	Cold Shield, Cylinder	ACAD
300002M101	2/28/2020	Cold Shield, Top Plate	ACAD
300002M102	9/19/2022	Cold Shield, Bottom L-Bracket	ACAD
300002M103	9/19/2022	Cold Shield, Top L-Bracket	ACAD
300002M104	8/13/2021	Cold Straps	ACAD
300002M105	11/16/2021	Cold Strap To Coax Clamp	ACAD
300002M106	8/31/2021	15 K Stage Assembly, Base Plate	ACAD
300002M107	8/31/2021	15 K Stage Assembly, Cold Strap Hub	ACAD
300002M108	8/31/2021	15 K Stage Assembly, Charcoal Plate	ACAD
300002M109	6/23/2021	Cal Kit, WR90 To 0.900 Square Adapter	ACAD
300002M110	1/31/2020	Cal Kit, 0.900 Square Delay	ACAD
300002M111	1/31/2020	Cal Kit, 0.900 Square Short	ACAD
300002M112	1/31/2020	Cal Kit, WR90 Delay	ACAD
300002M113	1/31/2020	Cal Kit, WR90 Short	ACAD
300002M114	2/17/2021	Cal Kit, 0.900 Square To 0.947 Square Adapter, Bottom	ACAD
300002M115	2/17/2021	Cal Kit, 0.900 Square To 0.947 Square Adapter, Top	ACAD
300002M116	3/16/2021	Cal Kit, 0.947 Square Delay	ACAD
300002M117	3/16/2021	Cal Kit, 0.947 Square Short	ACAD
300002M118	4/15/2021	Cal Kit, Circular Delay	ACAD
300002M119	4/15/2021	Cal Kit, Circular Short	ACAD
300002M120	2/4/2021	Cal Kit, Circular Flange Centering Ring	ACAD
300002M121	5/14/2021	Cal Kit, Feed Horn Test Adapter Plate	ACAD
300002M122	6/7/2021	Cal Kit, Feed Horn Delay	ACAD
300002M123	6/7/2021	Cal Kit, Feed Horn Short	ACAD
300002M124	6/7/2021	Cal Kit, Feed Horn Centering Ring	ACAD
300002M125	7/3/2023	Card Cage Fan Plate	ACAD
300002M126	7/3/2023	Card Cage Fan Plate Hinge	ACAD
300002M127	7/3/2023	Card Cage Fan Plate Handle	ACAD
300002M128	12/4/2021	Downconverter Ad590 Temp Sensor Block	ACAD

Table 16. PCB layouts

Dwg. no.	Dwg. date	Dwg. title	Frmt.
300002Q001	12/3/2021	Voltage Scaling Board	Eagle
300002Q002	3/18/2021	Voltage Regulator Board	Eagle
300002Q003	5/26/2021	Led Indicator Board	Eagle
300002Q004	3/26/2022	Fanout Board	Eagle
300002Q005	2/5/2022	Inverter Board	Eagle
300002Q006	2/4/2022	AD590 Temp Sensor Output Board	Eagle
300002Q007	2/5/2022	LO Power Detector Output Board	Eagle
300002Q008	4/28/2021	Transfer Switch Bias Board	Eagle

Table 17. PCB schematics

Dwg. no.	Dwg. date	Dwg. title	Frmt.
300002S001	5/7/2020	Voltage Scaling Board	Eagle
300002S002	4/15/2021	Voltage Regulator Board	Eagle
300002S003	5/25/2021	Led Indicator Board	Eagle
300002S004	3/26/2022	Fanout Board	Eagle
300002S005	2/5/2022	Inverter Board	Eagle
300002S006	2/2/2022	AD590 Temp Sensor Output Board	Eagle
300002S007	2/1/2022	LO Power Detector Output Board	Eagle
300002S008	5/20/2021	Transfer Switch Bias Board	Eagle

Table 18. Wiring lists

Dwg. no.	Dwg. date	Dwg. title	Frmt.
300002W001	11/3/2023	Wiring List	Word

14. Troubleshooting

14.1. Spurs

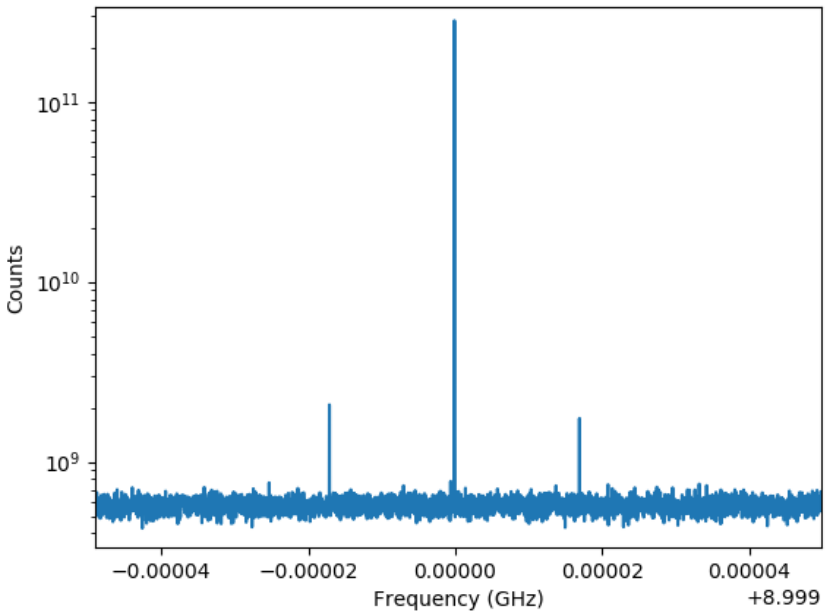

Fig. 35.— 8.999 GHz test tone injected into the X-band receiver phase cal port being amplitude modulated as a result of near-thermal-shutdown in the voltage regulators supplying power to the downconverter module's amplifiers. Conditions approaching thermal shutdown have been observed to modulate the voltage regulator output current at about 17 kHz, which is the separation of the sideband tones from the main test tone.

The appearance of spurious tones (spurs) at the output of the receiver can come from a few known sources:

- LO leakage to IF port of mixers
- Cavity mode resonances in downconverter module
- Thermal shutdown of voltage regulators on voltage regulator card

The first source is easily identifiable, because the spur frequency will match the LO frequency or one of its harmonics. The mechanism for the leakage is due to the coupling of the LO into the cavity modes of the downconverter module, as described in Section 11. Unmitigated, the LO leakage has been observed to be about 0 dBm with a nominal LO drive level (∼0 dBm to the downconverter

module LO input). Suppressing these modes can be accomplished by adding additional shielding or absorber material on the underside of the module's lid. The shields offered by X-Microwave (part number XM-SHIELD-01) and absorber material offered by Cuming Microwave (part number C-RAM GDSS) have both been used for this purpose, but adjustment of their position may be required.

Cavity mode resonances work similarly to the above mechanism, although they need not be excited by a strong tone, and so the resulting spur frequency may not correspond to any tones at the inputs to the downconverter module. Their frequency will likely exceed the cavity's unloaded cutoff frequency of 10.9 GHz, and their strength may be comparable to that of the LO leakage described above. Suppressing these spurs can also be accomplished with added shielding or absorber material.

Spurs may also result from the voltage regulators supplying power to the downconverter module amplifiers entering or approaching thermal shutdown. Under these conditions, the output current from the regulator will be rapidly switched or modulated, which in turn manifests as an amplitude modulation of any expected tone appearing at the downconverter module output. With sufficiently high spectral resolution, this can be observed as a pair of smaller tones on either side of the expected tone, where the spacing is equal to the current modulation frequency (usually in the kHz range). An example of these spurious tones and the corresponding current modulation is shown in Figures 35 and 36, respectively. Under normal operating conditions, the regulators should be sufficiently cool to avoid thermal shutdown. If it does occur, however, possible causes may be that the card cage fan has been shut off or failed or the temperature in the receiver room has increased substantially.

A. Combined cross-polarization due to phase shifter, 45 degree twist, and OMT

The X-band receiver uses a series cascade of waveguide elements, a phase shifter, 45 degree twist, and OMT, to separate received right- and left-circularly polarized waves into two channels. The combined cross-polarization due to these three components can be estimated from their individual sets of measured S-parameters. A signal flow graph representation for the combined effect on an incident power wave is shown in Figure 37 in terms of these S-parameters. Here, a_x and a_y are the two orthogonal linearly polarized components of the wave incident at the phase shifter input, where the x and y axes are oriented along either of the two inner walls of the phase shifter waveguide. The output power wave of the OMT consists of linearly polarized and spatially separate components b_R and b_L, where the R and L indices denote to the dominant circular polarization at the phase shifter input which drives either OMT output port.

A few simplifying assumptions have been made in order to produce the flow graph in Figure 37. One is that the input of the phase shifter and the output of the OMT are perfectly matched to the adjoining components. A second assumption is that the only non-negligible "cross-terms" which cross-couple the two polarizations are S_{L1x}^{OMT} and S_{R1y}^{OMT} and all others (which were not measured) can be omitted along with all remaining branches and nodes not contributing to the outputs b_R

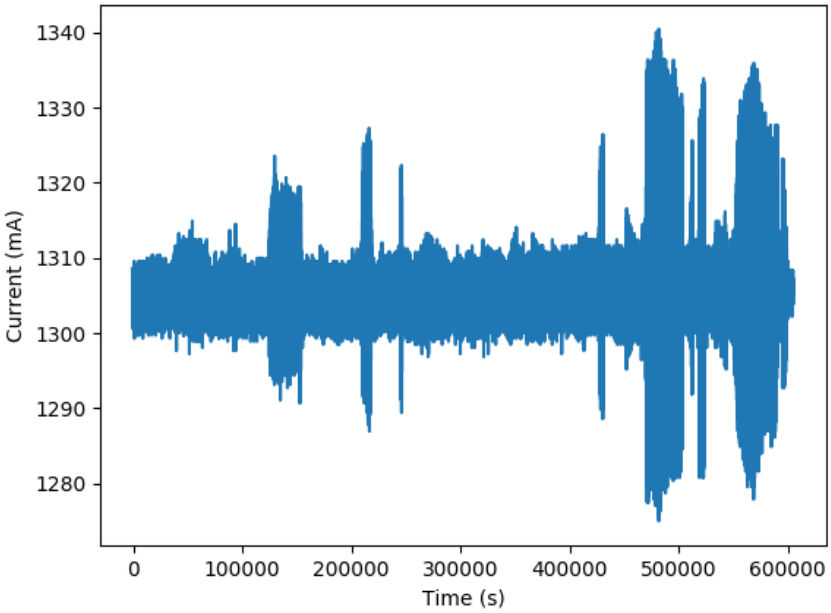

Fig. 36.— Total current supplied to all four RF amplifiers in downconverter module. Intermittent periods of increased fluctuation are associated with the voltage regulators supplying the amplifiers with power approaching thermal shutdown.

and b_L. Finally, it should be noted that the OMT S-parameters must first be transformed from the measured S-parameters $\mathbf{S}^{OMT'}$, since for the latter the modes driven at the OMT input were polarized along axes u and v oriented parallel to either of the sides of the input port, whereas the x and y axes defined above are oriented at 45 degrees to the sides of the input port. The relevant transformation is the following:

$$\mathbf{S}^{OMT} = \mathbf{R}^{\mathrm{T}}\mathbf{S}^{OMT'}\mathbf{R}, \tag{A1}$$

$$\mathbf{R} = \begin{bmatrix} \sqrt{\frac{1}{2}} & 0 & -\sqrt{\frac{1}{2}} & 0 \\ 0 & 1 & 0 & 0 \\ \sqrt{\frac{1}{2}} & 0 & \sqrt{\frac{1}{2}} & 0 \\ 0 & 0 & 0 & 1 \end{bmatrix}, \tag{A2}$$

where the left-to-right and top-to-bottom ordering of the row and column indices for $\mathbf{S}^{OMT}$ and $\mathbf{S}^{OMT'}$ are, respectively, $\{1x, R, 1y, L\}$ and $\{1u, R, 1y, L\}$. The total cross-polarization from these three components can then be calculated by, for example, assuming the input to the phase shifter is right-circularly polarized (i.e. $a_x = 1/\sqrt{2}$ and $a_y = -i/\sqrt{2}$), using the flow graph to express b_R

and b_L in terms of the input and component S-parameters, and calculating the ratio $|b_L/b_R|$:

$$\begin{aligned}
\left|\frac{b_L}{b_R}\right| &= \left|\frac{AS^{OMT}_{L1x}a_x + BS^{OMT}_{L1y}a_y}{AS^{OMT}_{R1x}a_x + BS^{OMT}_{R1y}a_y}\right|, \\
&= \left|\frac{AS^{OMT}_{L1x} - iBS^{OMT}_{L1y}}{AS^{OMT}_{R1x} - iBS^{OMT}_{R1y}}\right|, \\
A &= \frac{S^{PS}_{2x1x}S^{45}_{2x1x}}{1 - \frac{S^{PS}_{2x2x}S^{45}_{1x2x}S^{45}_{2x1x}S^{OMT}_{1x1x}}{(1-S^{PS}_{2x2x}S^{45}_{1x1x})(1-S^{OMT}_{1x1x}S^{45}_{2x2x})}} \\
B &= \frac{S^{PS}_{2y1y}S^{45}_{2y1y}}{1 - \frac{S^{PS}_{2y2y}S^{45}_{1y2y}S^{45}_{2y1y}S^{OMT}_{1y1y}}{(1-S^{PS}_{2y2y}S^{45}_{1y1y})(1-S^{OMT}_{1y1y}S^{45}_{2y2y})}}
\end{aligned} \tag{A3}$$

A plot of this ratio over the range 7-13 GHz is shown in Figure 15.

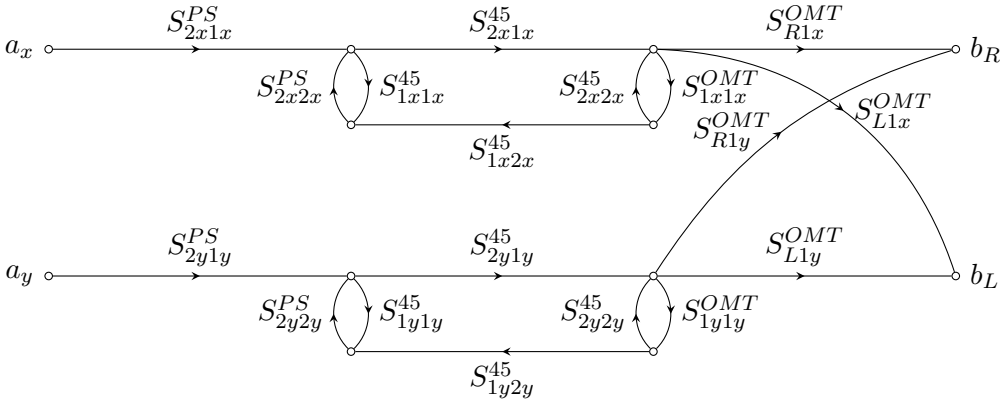

Fig. 37.— Simplified signal flow graph representation for the cascade of phase shifter, 45 degree twist, and OMT, with respective S-parameters S^{PS}_{ij}, S^{45}_{ij}, S^{OMT}_{ij} (where a given port supports more than one polarization, indices i and j denote both port number and linear polarization).

REFERENCES

ANSI/IEEE 1979, IEEE standard test procedures for antennas, Tech. Rep. 149-1979

doi: 10.1109/IEEESTD.1979.120310

De Pree, C., Armentrout, W., Beasley, T. et al. 2023, NRAO, RFI Memo 154

https://library.nrao.edu/public/memos/rfi/RFI_154.pdf

FCC 2022, FCC online table of frequency allocations

https://transition.fcc.gov/oet/spectrum/table/fcctable.pdf

Humphreys, T. E., Iannucci, P. A., Komodromos, Z. M., & Graff, A. M. 2023, ITAES, 59, 6016

doi: 10.1109/TAES.2023.3268610

Mason, B. S., 2013, NRAO, GBT Memo 282

https://library.nrao.edu/public/memos/gbt/GBT_282.pdf

Morgan, L., 2023, GBO, GBT Memo 314

https://library.nrao.edu/public/memos/gbt/GBT_314.pdf

Norrod, R. & Srikanth, S. 1996, NRAO, GBT Memo 155

https://library.nrao.edu/public/memos/gbt/GBT_155.pdf

Srikanth, S. 1993, NRAO, GBT Memo 102

https://library.nrao.edu/public/memos/gbt/GBT_102.pdf

Srikanth, S. 1997, IMGWL, 7, 150

doi: 10.1109/75.585196

Thomas, B. MacA. 1971, IEEEP, 118, 1539

doi: 10.1049/piee.1971.0282

Tiuri, M. 1964, ITAP, 12, 930

doi: 10.1109/TAP.1964.1138345

Weimer, B. D. 2020, Application for fixed satellite service by WorldVu Satellites Ltd., Debtor-in-Possession, SAT-MPL-20200526-00062

https://fcc.report/IBFS/SAT-MPL-20200526-00062

Wiltshire, W. 2020, Application for fixed satellite service by Space Exploration Holdings, LLC., Tech. Attachment SAT-LOA-20200526-00055

https://fcc.report/IBFS/SAT-LOA-20200526-00055